



HAL
open science

UAV and LiDAR Data in the Service of Bank Gully Erosion Measurement in Rambla de Algeciras Lakeshore

Radouane Hout, Véronique Maleval, Gil Mahe, Eric Rouvellac, Rémi Crouzevialle, Fabien Cerbelaud

► **To cite this version:**

Radouane Hout, Véronique Maleval, Gil Mahe, Eric Rouvellac, Rémi Crouzevialle, et al.. UAV and LiDAR Data in the Service of Bank Gully Erosion Measurement in Rambla de Algeciras Lakeshore. Water, 2020, 10.3390/w12102748 . hal-03035379

HAL Id: hal-03035379

<https://hal.science/hal-03035379>

Submitted on 2 Dec 2020

HAL is a multi-disciplinary open access archive for the deposit and dissemination of scientific research documents, whether they are published or not. The documents may come from teaching and research institutions in France or abroad, or from public or private research centers.

L'archive ouverte pluridisciplinaire **HAL**, est destinée au dépôt et à la diffusion de documents scientifiques de niveau recherche, publiés ou non, émanant des établissements d'enseignement et de recherche français ou étrangers, des laboratoires publics ou privés.

UAV and LiDAR Data in the Service of Bank Gully Erosion Measurement in Rambla de Algeciras Lakeshore

Radouane Hout ^{1*}, Véronique Maleval ¹, Gil Mahe ², Eric Rouvellac ¹, Rémi Crouzevialle ¹
and Fabien Cerbelaud ¹

¹ Department of Geography, Faculté des Lettres et Sciences Humaines, Limoges University, 39E rue Camille Guérin, 87036 Limoges CEDEX, France; veronique.maleval@unilim.fr (V.M.); eric.rouvellac@unilim.fr (E.R.); remi.crouzevialle@unilim.fr (R.C.); fabien.cerbelaud@unilim.fr (F.C.)

² IRD, UMR HSM IRD, University Montpellier, 34090 Montpellier, France; gil.mahe@ird.fr

* Correspondence: radouane.hout@unilim.fr; Tel.: +33-7-69-21-47-85

Abstract: The Rambla de Algeciras lake in Murcia is a reservoir for drinking water and contributes to the reduction of flooding. With a semi-arid climate and a very friable nature of the geological formations at the lakeshore level, the emergence and development of bank gullies is favored and poses a problem of silting of the dam. A study was conducted on these lakeshores to estimate the sediment input from the bank gullies. In 2018, three gullies of different types were the subject of three UAV photography missions to model in high resolution their low topographic change, using the SfM-MVS photogrammetry method. The combination of two configurations of nadir and oblique photography allowed us to obtain a complete high-resolution modeling of complex bank gullies with overhangs, as it was the case in site 3. To study annual lakeshore variability and sediment dynamics we used LiDAR data from the PNOA project taken in 2009 and 2016. For a better error analysis of UAV photogrammetry data we compared spatially variable and uniform uncertainty models, while taking into account the different sources of error. For LiDAR data, on the other hand, we used a spatially uniform error model. Depending on the geomorphology of the gullies and the configuration of the data capture, we chose the most appropriate method to detect geomorphological changes on the surfaces of the bank gullies. At site 3 the gully topography is complex, so we performed a 3D distance calculation between point clouds using the M3C2 algorithm to estimate the sediment budget. On sites 1 and 2 we used the DoD technique to estimate the sediment budget as it was the case for the LiDAR data. The results of the LiDAR and UAV data reveal significant lakeshore erosion activity by bank gullies since the annual inflow from the banks is estimated at 39 T/ha/year.

Keywords: Rambla de Algeciras; semi-arid; lake; lakeshores; silting; bank gullies; UAV; LiDAR; DoD; M3C2

1. Introduction

Gully erosion is a very common form of water erosion, this geomorphological process is triggered after the concentration of surface or groundwater in narrow areas. This drags soil particles and rock fragments from these narrow flow paths to considerable depths. The steep slopes, the low density of plant cover, the overexploitation of arable lands, overgrazing as well as the torrential flow regime due to irregular rainfall, are all factors favorable to the initiation and even the acceleration of the gully erosion phenomenon [1–3].

This process of global erosion occurs in urban, forest and even rural areas [4]. That is why we find the term “gully” depicted in several languages, it is called, “Ravine” in French, “wadi” in Arabic, “cárcava” in Spain, “lavaka” in Madagascar, “donga” in South Africa, “voçoroca” in Brazil and “barranco” in Argentina [4].

Globally, gullying accounts for 10% up to 94% of the total sediment yield produced by water erosion [5], with an average contribution of 50% to 80% in arid areas [6]. In Western European countries, the same process generates between 30 and 80% [5] of the sediment.

Bank gullies are themselves a very particular form of gullies which are formed after a height drop from terraces or river banks, the lake banks, and which develop by headward retreat in erodible hillslopes. Bank gullies are themselves a very particular form of gullies which are formed after a height drop from terraces or river banks, the lake banks, and which develop by headward retreat in erodible hillslopes.

Furthermore, Vanmaercke et al (2016) [7] have demonstrated that gullying and bank gullies are the main sources of sediment loss. It is also important to note that they also have off-site effects [8] such as degradation of water quality, siltation of dams, pollution, degradation of agricultural land, reduction of soil moisture, hydrological dysfunction, and even fertility transfers [9]. Vanmaercke et al (2016) [7] confirmed that the recession rate of bank gullies heads varies between 0.01 m/year and 135.2 m/year with an average of 5 m/year, and a median of 0.89 m/year in Spain. In most landscapes that are subject to different climatic conditions and different anthropogenic activities, we can observe the presence of various forms of gully erosion, namely ephemeral gullies, permanent or classic gullies and bank gullies [5].

In the literature, researchers address the question of gullying according to different approaches:

- Approach based on the quantitative estimation of the sediment balance, using direct measurements in the field, namely, measuring tape, total station (TS), DGPS (differential GPS), drone (UAV), LiDAR, etc. [10];
- Indirect approach based on the modeling of the gully's sub-processes, by numerical or statistical gully forecasting models such as the SCS (Soil Conservation Service) model [11], the Thompson models [12,13], AnnAGNPS [14], EGEM (Ephemeral Gully Erosion Model) [15], GULTEM (model to Predict Gully Thermoerosion and Erosion) [16], or CHILD (Channel-Hillslope Integrated Landscape Development) [17].

The work of Evans [18] has shown that the activity of bank gullies lead to the evolution of hillslope-channel coupling related to flow erosion. In Morocco, the work of Maleval [19] demonstrated the importance of sedimentary inputs from the bank gullies in the silting of the SMBA dam. Monitoring and mapping of gullies for lakeshores remain one of the very important objectives in the management of drinking water reservoirs. Very high resolution topographic acquisitions have considerably improved our ability to better understand the functioning and evolution of geomorphological changes in the shoreline. The emergence of new drone photography techniques in recent years has greatly facilitated digital terrain modeling and geomorphological analysis. This ease is mainly due to the appearance of civil drones (Unmanned Airborne Vehicles, UAVs) and to SfM-MVS 3D photogrammetry algorithms, but also to the development of the computational capacity of computers. This method is increasingly being used for modeling and quantifying gullying in several regions of the world and in various climatic contexts, with work carried out in Morocco [20], Spain [21], China [22], Italy [23], Ethiopia [24], the United States [25], Australia [26], etc.

In this paper, the gullies for lakeshores of the Rambla de Algaciras dam have been mapped using UAV and LiDAR. Our objective was to understand the influence of gullies for lakeshores in the silting of artificial dams using 4D models and photo-interpretation of aerial photos. A detailed methodology for the collection, processing and validation of very high resolution 4D models has been developed to quantify sediment budgets and geomorphological changes of lake bank gullies in the short and medium term. The topographic complexity of certain bank gullies was taken into account in this work through a combination of oblique and vertical acquisition of aerial photos.

In this article we also measured the accuracy of digital terrain models taken by UAVs with the k-fold cross-validation method, to estimate the sediment budget on bank gullies using the DoD method and the M3C2-PM algorithm. The conclusions of this study will guide dam managers to implement

several strategies to take into account the contributions of bank gullies which are generally underestimated in the hydro-sediment balances.

2. Methodology

2.1. Study Site

In the south of Spain, in Alhama de Murcia, the Rambla de Algeciras reservoir was built in 1995 on the Rambla de Algeciras river. It has a torrential character, it rises at the gully of Valdelaparra and flows into the Guadalentín river. The dam is 80 m high and the area of the lake is 235.50 ha and 42.13 hm³ (Figure 1). The dam was built under the project “Plan General de Defensa contra Avenidas de la Cuenca del Segura”, intended to develop and regularize water resources in the Segura watershed in south-eastern Spain. The Rambla de Algeciras dam is located in the catchment area by the same name, southwest of the city of Murcia at the northern limit of the depression of the Guadalentín river (left bank). Surrounded by las sierras del Cura, de Espuña and La Muela. This watershed covers an area of 44.91 km², and 15 km, with an altitude that varies between 200 and 1320 m above sea level. It undergoes a high rate of erosion reaching 100 t/ha/year (Global Atlas of the Murcia region 2002), linked to the torrential nature of precipitation and the detrital nature of the soil composed of marls and polygenic conglomerates.

Locally, Lake Rambla de Algeciras has a semi-arid climate, with short episodes of intense precipitation. Annual rainfall 393 mm, 60% of which is concentrated over 3 to 4 days/year.

The lakeshore and substrate of the Rambla de Algeciras dam are made up of different friable formations of the Tortonian period, on the banks of the lake we find blue loams interspersed with whitish calcareous loams and gypsiferous loams in discordance with calcarenite and molasses formations, on the right bank of the dam we note the presence of alternating soft and consolidated layers of polygenic conglomerates in a marly sand matrix.

The choice of gullies aimed to represent as faithfully as possible the erosion activity on the lakeshore, in a semi-arid climatic context. This choice takes into account several parameters such as the shape, the exposure, the head of the gullies, the density of the plant cover, and the lithology. Based on the diachronic photo-interpretation of aerial photos (PNOA), three gullies models were selected (Figure 1).

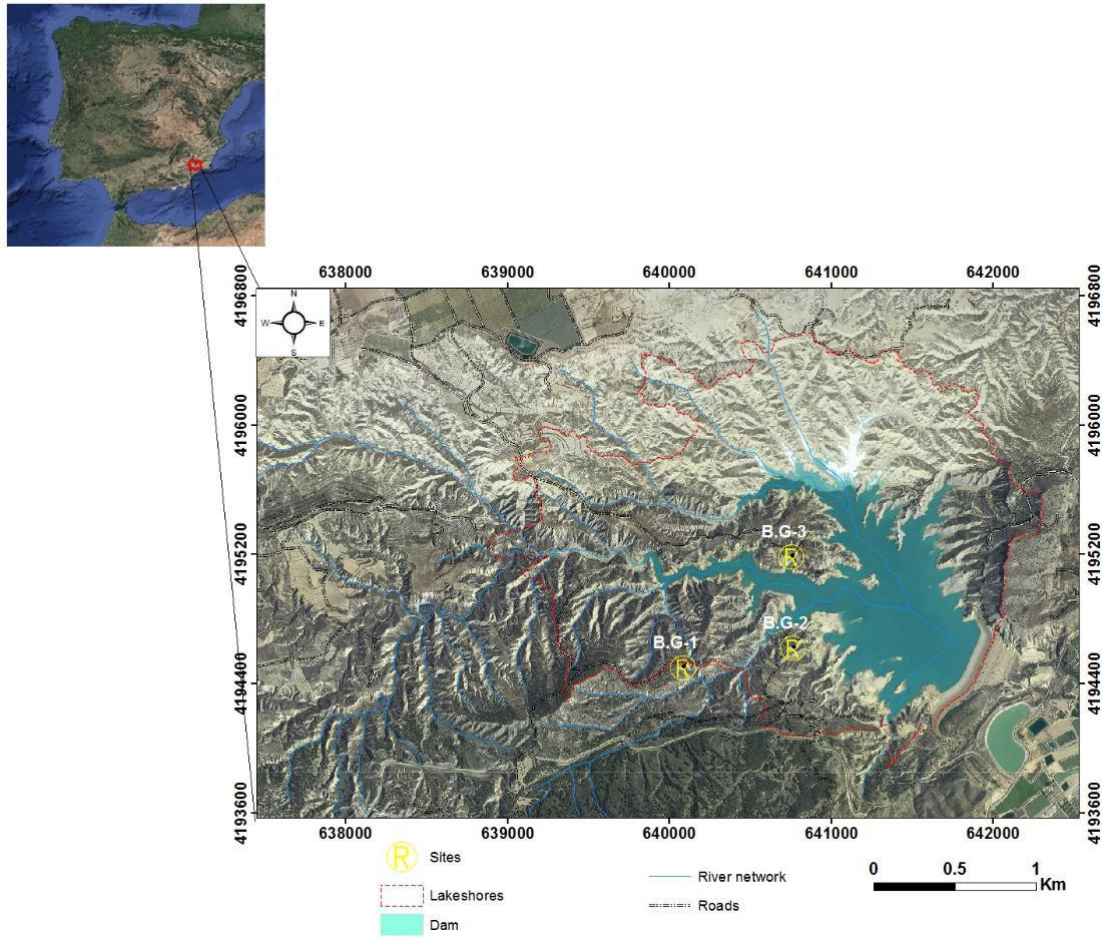


Figure 1. Location of the study area.

2.1.1. Site 1

The bank gully (B.G-1) (Figure 2C), extends over approximately 130 m. It is V-shaped in the upper and middle part, then takes a U-shape downstream from the gully, where the slopes are steep and exposed to the East (low grass cover) or to the West (bare soil). Upstream of the gully (head) is covered by tree layers, planted as part of the restoration project (Proyecto de correccion y repoblacion forestal de las cuencas de las Ramblas de Belen, Librillas y Algeciras. Provincia de Murcia). The North-south oriented gullies have been reforested and are difficult to access. Thus we studied the B.G-1 which is located 250 m from the reservoir. Access to the bank gully of the lakeshore protected by the forest cover and is very difficult. It is for this reason that we chose site B.G-1 which is located at 250 m from the lake.

2.1.2. Site 2

The second bank gully (B.G-2)(B.G-1) (Figure 2D) is U-shaped. It is oriented East-west with very steep slopes facing North (herbaceous vegetation) and South (bare soil). It is 110 m long, and receives tributary gullies.

2.1.3. Site 3

The third bank gully (B.G-3)(B.G-1) (Figure 2B) has a complex shape and is the result of a combination of tunnel gullying (pipig). The slopes of the gully (B.G-3) covered by bare soil. According to photo-interpretation, the B.G-3 gully began to develop after the lake level receded. It's likely to turn into badlands.

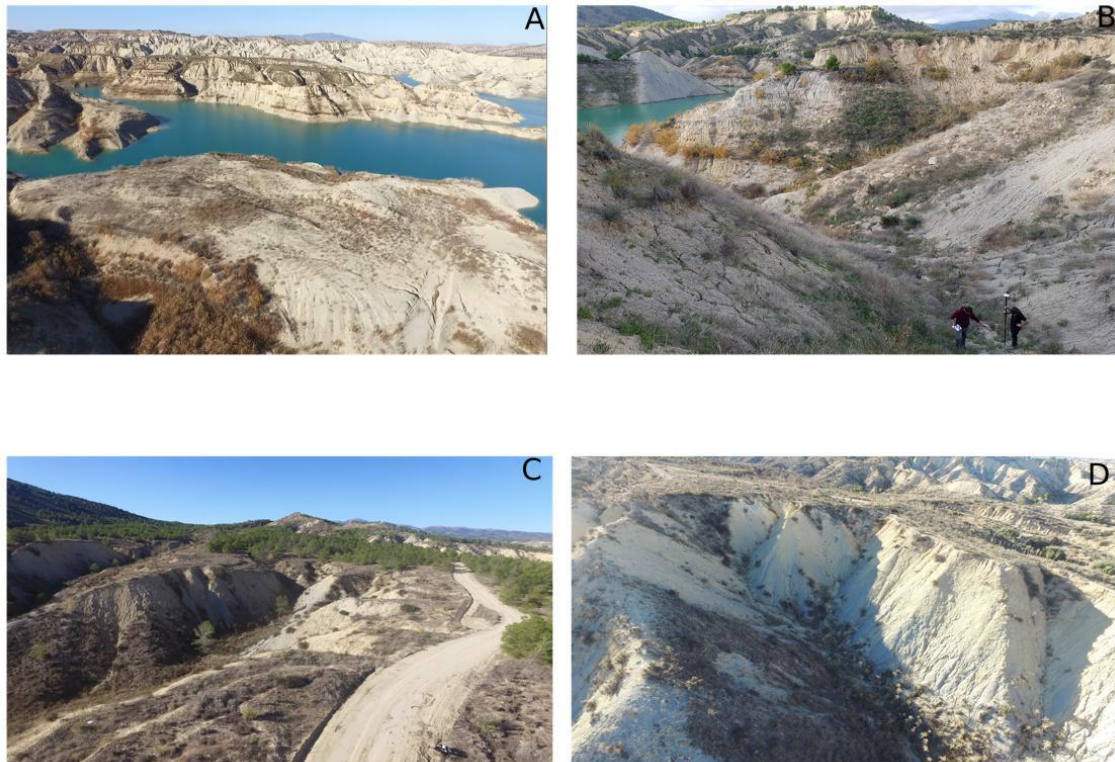


Figure 2. Photos of the lakeshore of Rambla de Algeciras. **(A)** Lakeshore. **(B)** Third bank gully. **(C)** Bank gully (B.G.-1). **(D)** Second bank gully.

2.2. Precipitation Analysis

2.2.1. Rainfall Extremes

Rare and very rare extreme events were identified using the prec90p index, of the STARDEX project (Statistical and Regional Dynamical downscaling of Extremes for European regions). The prec90p index is used to determine heavy rain events and intense rain when the cumulative daily precipitation values are greater than or equal to 90 and 95 percentiles, respectively. Between 2009 and 2016 there were two heavy showers (Figure 3).

- 7 June 2011, with cumulative precipitation of 81 mm in 2 h and a high intensity of precipitation which exceeds 40 mm/h.
- 28 September 2012, with cumulative precipitation was 84 mm produced in 4 h and an intensity of 21 mm/h.

These two rain events are considered as extreme events and automatically play an important role in erosion. The modification of the precipitation regime with the decrease in the amount of precipitation and rainy days as well as the greater frequency of rare and very rare events during the eight years of topographic surveys can be explained by the effect of climate change in the Mediterranean area [27].

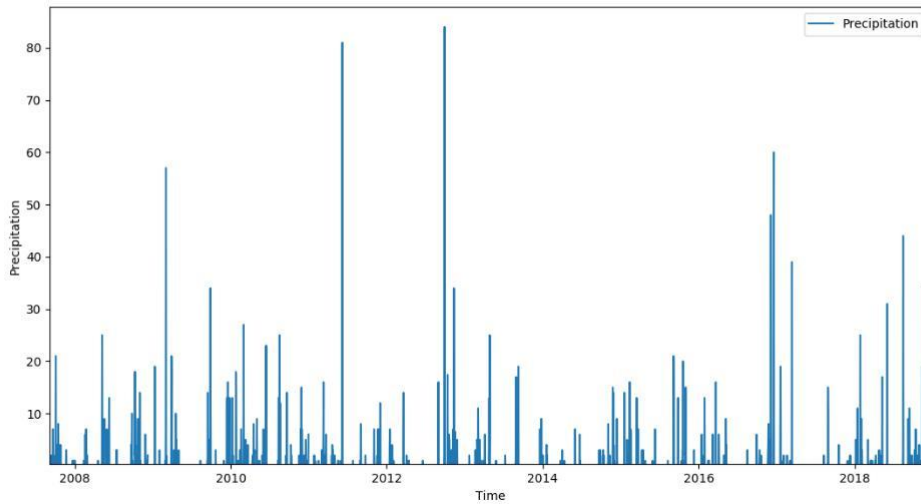


Figure 3. Rain event between 2009 and 2019 in the station of Rambla de Algeciras.

2.2.2. Rainfall Erosivity Factor “R-Factor”

The R-factor was estimated using equation (Equation (1)) (zone-2) proposed by ICONA for the region of Murcia. The monthly analysis of the factor R traces the evolution of the aggressiveness of the rains on the gullies between the study period of 2009 and 2016 as well as for the year 2018. Between 2009 and 2016 the devastating activity of the rains is concentrated annually in March and September. This activity is linked to the increase in intense rain events during this period. Throughout the period 2009 to 2016, the R-factor peaks are recorded in June 2011 and September 2012, which coincides with an anomaly in the kinetic energy explained by the recording of two extreme phenomena. The year 2018 is relatively wet therefore implying a natural increase in the factor R. From the graph (Figure 4) we can see that the average value of R, calculated for the wet season, is quite low compared to that of the dry season. During the wet season the values of (R) are moderate with an average of $8.8 \text{ MJ cm ha}^{-1} \text{ h}^{-1} \text{ year}^{-1}$, through contribution of the season which recorded an average of $17 \text{ MJ cm ha}^{-1} \text{ h}^{-1} \text{ year}^{-1}$. The lowest values are recorded between February and April. Conversely, during the dry season, the highest cumulative value of R is $102 \text{ MJ cm ha}^{-1} \text{ h}^{-1} \text{ year}^{-1}$, and it is associated with very intense precipitation in August and November. R: Climate aggressiveness ($\text{MJ cm ha}^{-1} \text{ h}^{-1} \text{ year}^{-1}$) PMEX: The maximum monthly value (mm) MR: Cumulative precipitation between October–May (mm) MV: Cumulative precipitation between June–September (mm):

$$R = e^{1.235} \text{ PMEX}^{1.297} \text{ MR}^{0.511} \text{ MV}^{0.366} \text{ F}_{24}^{0.414} \quad (1)$$

where

R: Rainfall erosivity factor ($\text{MJ cm ha}^{-1} \text{ h}^{-1} \text{ year}^{-1}$)

PMEX: Maximum monthly pre-cipitation (mm) MR:

Total rainfall from October to May (mm)

MV: Total rainfall from June–September (mm)

F₂₄: Ratio of the square of the maximum annual rainfall in 24 hours (mm) to the sum of the maximum monthly rainfall in 24 hours (mm) $F_{24} = \frac{(P_{24h,annual})^2}{\sum_{i=1}^{12} P_{24h,i}}$

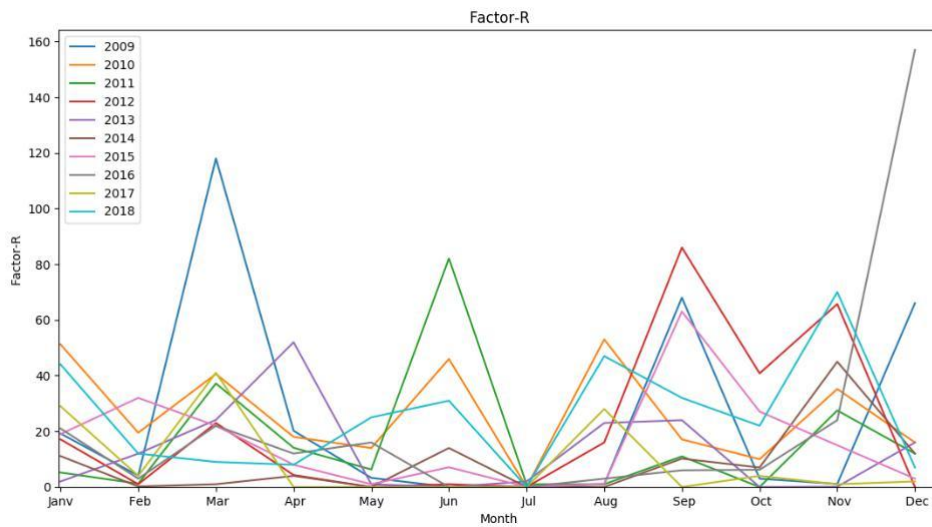


Figure 4. R-factor.

2.3. UAV Data Processing

2.3.1. UAV Data Collection

The aerial photography missions were carried out easily and at low cost by the quadrotor drone DJI Inspire 1 v2 (Figure 5A), equipped with the metric and multispectral camera ZENMUSE X3 without distortion or aspect and with a focal distance of 20 mm (Figure 5D). The DJI Inspire1 V2 is sold “Ready-To-Fly”, and is designed to have a maximum speed of 22 m/s (ATTI mode, no wind), and a maximum flight time of approximately 18 min. It can reach 2500 m altitude in flight. In addition, it is equipped with a satellite positioning system which uses GLONASS and GPS system.



Figure 5. (A) Drone DJI Inspire 1 v2. (B) GPS Trimble Geo 7x. (C) Ground control points. (D) Camera ZENMUSE X3.

Flight mission planning was done in navigation mode via the Pix4Dcapture mobile application. After the definition of some flight parameters (flight plan, flight altitude, recovery rate, shooting angle, starting and arrival point of the UAV) the application automatically pilots the UAV. The acquisitions of aerial photos by drone were carried out according to two configurations, for the two gullies (B.G 1 and 2) the photos were taken nadir acquisitions. However, by geomorphological constraints of having gully (B.G-3) we combined the two modes of acquisition nadir and oblique at (30°) in order to model in 3D the overhanging areas of the gully (B.G-3). To ensure a successful photographic reconstruction we have chosen a longitudinal overlap of 80% and a lateral overlap of 60% to avoid gaps between the different photographs. A minimum of 10 ground control points (GCPs) (Figure 5C) (Table 1) is required on each site in the middle and at the stable edge, and the same targets were used in each drone mission (except for those which were covered by the sediments), in order to obtain optimal results. The surveys were carried out by the GPS Trimble Geo 7x (Figure 5B), which includes the following parameters: the ellipsoid GRS 1980, the datum: European Terrestrial Reference System 1989, coordinate system: ETRS89 / UTM zone 30N, with a horizontal accuracy of 1 cm + 1 ppm, and vertical of 1.5 cm + 2 ppm. We used the Stop&Go kinematic approach for the collection of GCPs points. We then made subsequent corrections using RINEX data from a reference station located 30 km from our study area.

Table 1. Characteristics of UAV photo missions.

| | | | | | | | | | |
|-------|----------|------|----------|----------|----------|----------|----------|----------|----------|
| B.G-1 | 22/01/18 | 11 h | 27.6 | 02/08 | 436 | 517 | 2.95 | 7 | 90 |
| | 04/06/18 | 15 h | 36.4 | 01/08 | 304 | 408 | 2.34 | 7 | 90 |
| | 18/12/18 | 16 h | 27.5 | 03/08 | 422 | 524 | 2.7 | 7 | 90 |
| B.G-2 | 22/01/18 | 15 h | 31.3 | 02/08 | 646 | 425 | 4.3 | 13 | 90 |
| | 04/06/18 | 11 h | 29.4 | 01/08 | 465 | 455 | 1.79 | 13 | 90 |
| | 18/12/18 | 15 h | 30 | 03/08 | 384 | 397 | 2.02 | 10 | 90 |
| B.G-3 | 22/01/18 | 17 h | 37.4 | 02/08 | 741 | 394 | 2.28 | 16 | 90+30 |
| | 04/06/18 | 10 h | 28.9 | 01/08 | 520 | 433 | 1.28 | 14 | 90+30 |
| | 18/12/18 | 10 h | 33.3 | 03/08 | 602 | 328 | 2.5 | 11 | 90+30 |
| | | | 1 | 2 | 3 | 4 | 5 | 6 | 7 |

1: Flight height (m), 2: Cloud cover (Octas), 3: Number of images, 4: Density (pts/m²), 5: Coverage (Ha), 6: Number of GCPs, 7: Angle of acquisition (°)

2.3.2. Processing

The aerial photo processing is based on the SfM-MVS photogrammetry technique. We have chosen the Agisoft PhotoScan commercial software to process all the photos taken by the drone, eventually generating dense point clouds and orthomosaics. This software generates exportable datasets and thus has the most comprehensive and easy to use workflow compared to other commercial and open source photogrammetry software's. The following steps on PhotoScan consisted of establishing dense point clouds which we will then export in ASCII or PTS "XYZ RGB" format (Figure 6).

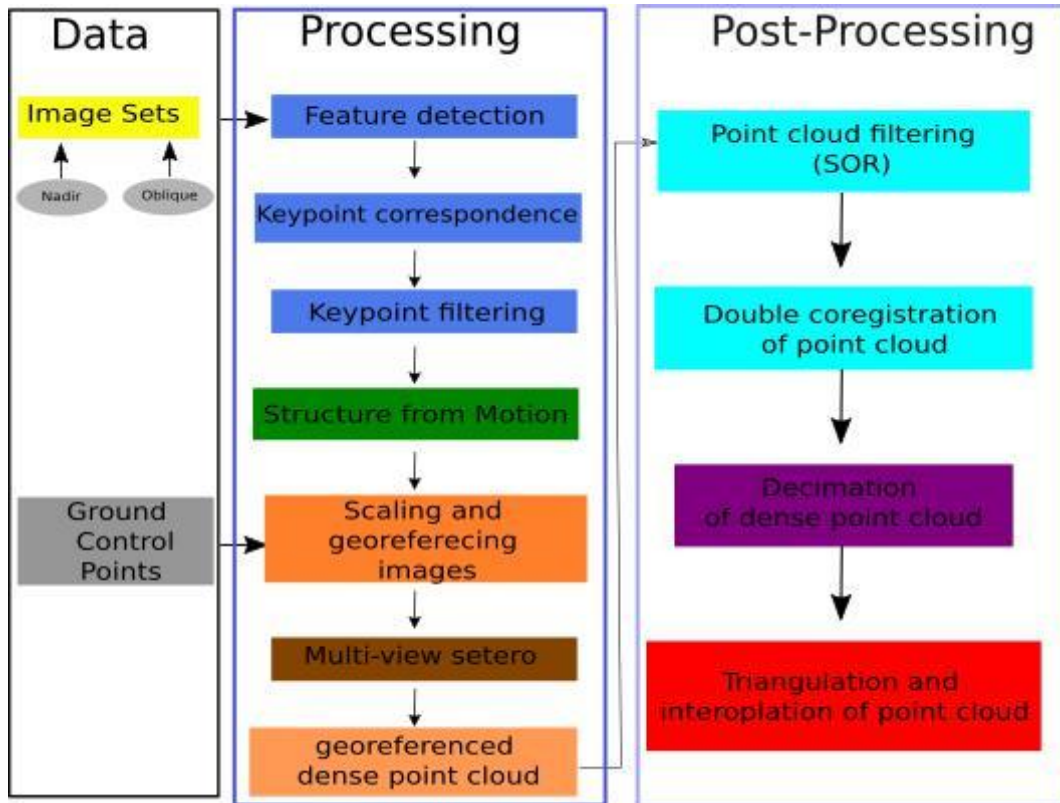


Figure 6. A schematic of a workflow that was applied to UAV data.

2.3.3. Post-Processing

The SfM-MVS technique is recognized as the fastest and inexpensive technique for 3D modeling. Post-processing was applied to the raw point clouds obtained by the SfM-MVS technique before generating the digital terrain model (Figure 6). The post-processing step was carried out by three open source external software: CloudCompare software (<http://www.cloudcompare.org/>), ToPCAT (<https://code.google.com/archive/p/point-cloud-tools/downloads>), and SAGA GIS software

Filtering and Coregistration of Data

CloudCompare open source software is designed for processing and comparing 3D point clouds. The dense 3D point clouds obtained were imported in ASCII XYZRGB formats into the CloudCompare software. We then filtered the point clouds using the SOR filter. Once the point clouds were filtered, we applied the ICP coregistration algorithm to match the homologous points of the multi-temporal point clouds, so that each dense point cloud would refer to the same area [28–32].

The Decimation and Interpolation of Point Clouds

Generating a digital terrain model from dense point clouds directly derived from MVS algorithms often requires large computing resources. The interpolation of the points for this kind of processing drains the machines in terms of memory, hence the interest for the decimation of the clouds of dense points which has the potential to reduce the number of points while preserving the topographic complexity of the soil surface. Persistent in the point cloud, we used the ToPCAT geospatial toolbox (Topographic Point Cloud Analysis Toolkit). ToPCAT is an intelligent analysis and decimation algorithm that breaks down the very dense point cloud into a set of non-overlapping meshes, suitable for detecting morphological changes. It then calculates the minimum elevation (Z_{min}) of each mesh. (Z_{min}) is considered to be the elevation of bare ground points [33–36]. The (Z_{min}) elevation obtained

was then converted to TIN (Triangular Irregular Networks) in order to generate the digital terrain model under the SAGA GIS software.

2.4. LiDAR-PNOA Data Processing

In the Murcia region, two ALS airborne LiDAR missions were conducted, on 24 November 2009 and between 20 and 25 August 2016 (Figure 7). During the first mission, data were collected using a Leica ALS50-II sensor, and for the second mission, data were collected using a Leica ALS60-II sensor.

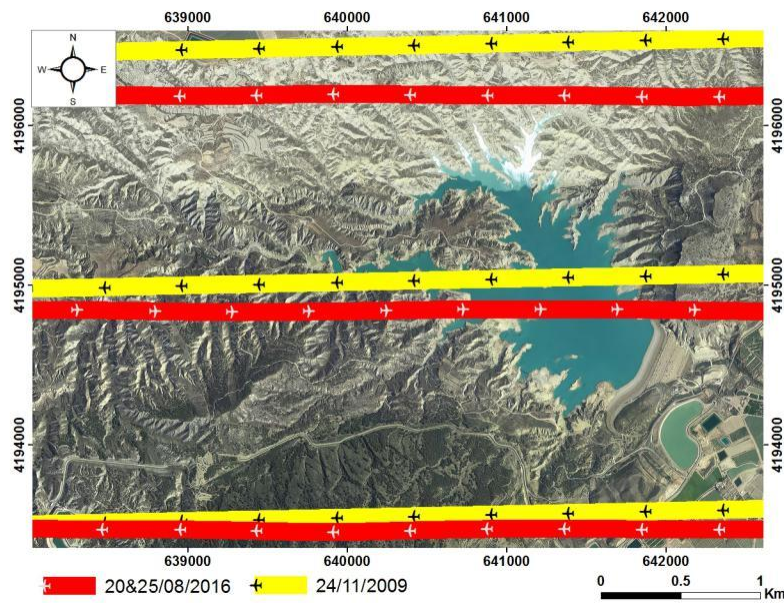


Figure 7. LiDAR flight turnings.

The LAZ files (binary file compression format LAS version 1.1) that we used come from the ETRS89 UTM Zone 30 geodetic reference system for X, Y and Z coordinates in the EGM08-REDNAP system. Before the classification of the LiDAR point cloud, we prepared the LiDAR raw data in the open source software LASTools. We first converted the LAZ files into LAS files using the las2las algorithm, then we applied a vertical and a horizontal alignment between the flight lines using the lasoverlap algorithm, and finally we transformed the point cloud into EGM08-REDNAP orthometric coordinates using the ascii file <EGM08-REDNAP.asc > and the lasheight algorithm.

Subsequently, we removed outliers and noise using the SOR filter in the CloudCompare software. After pre-processing the point cloud, we chose the MCC-LiDAR v2.15 (Multiscale Curvature Classification) application, an open source command line tool for processing LiDAR data. It classifies data points as ground or non-ground, using the MCC algorithm, to obtain a digital model of bare terrain. Due to the low density of PNOA LiDAR point clouds ranging from 0.5 to 1 point/m², we did not apply a mesh to the cloud.

Finally, the ground points were triangulated and then interpolated with the linear interpolation algorithm under the SAGA GIS software, in order to obtain two ground DTMs of 1 m resolution for 2009 and 2016.

2.4.1. Error Modeling

Cross Validation: K-fold Cross-Validation

It is likely that the roughness-based estimates are incorrect, For quantify spatially variable SfM-DEM uncertainty we used cross-validation, then the results of this technique will be integrated from a FIS error model more representative of the different sources of uncertainty. This statistical technique of resampling without replacement consists in dividing the decimated point cloud into validation (20%) and training data (80%) (Figure 8). The clouds are divided repeatedly with the k-

folds (k-fold cross validation) algorithm with a $k = 5$ (5 subsets of validation point cloud). The training points are interpolated to build a DEM, which compared the validation points in order to quantify the uncertainty of DEM-SfM. We chose the Scikit-Learn (v-0.22.0) free software machine learning library to apply k-fold cross validation on the point cloud decimated by the ToPCAT algorithm. 80% of the (Z_{min}) points were randomly selected to generate a DEM with a resolution of 5 cm. Then we used the remaining 20% of (Z_{min}) to compare them with the DEM. The average absolute difference is taken as an indicator of the altimetric uncertainty of the data. The cross-validation test was repeated five times to check the consistency of the results.

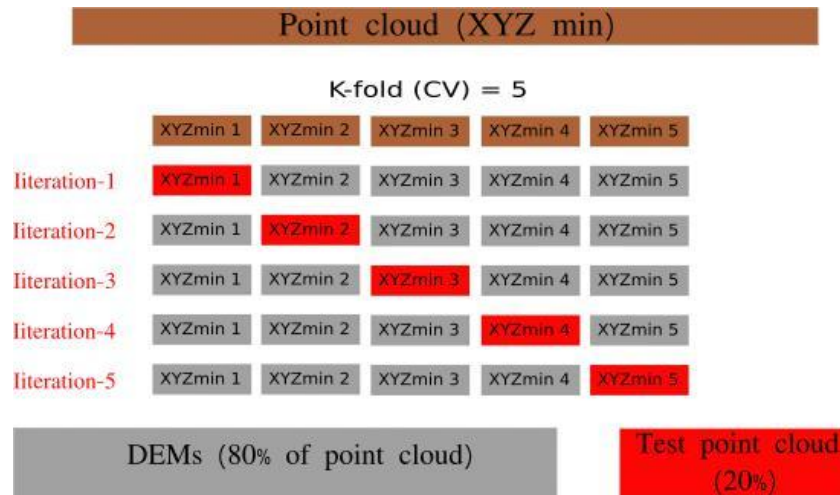


Figure 8. K-fold cross-validation model.

Fuzzy Inference System (FIS)

Within the SfM-MVS data, the sources of error vary according to the type of site. In the case of bank gullies, the main sources of error are roughness, slope of the terrain, camera geometry, interpolation error and point cloud density. In this case we were interested in a more comprehensive error modeling that takes into account the different sources of uncertainty. To meet the modelling requirements we adopted a spatially variable FIS (Fuzzy Inference System) error model, which is more reliable model errors in the SfM-MVS-4D data [35,37].

We defined four variables as the error sources of the SfM-MVS data to model with the FIS, namely slope, point density, interpolation error, and 3D point cloud error. Slope is the parameter most representative of the topographic complexity of the terrain, and it is the easiest parameter to derive from the DTM or point clouds. The slope (degrees) was generated directly from the decimated ' Z_{min} ' point clouds with a resolution of 5 cm.

The modeling of the bare ground roughness from the value of the standard deviation of the decimated dense point clouds $s_{Z_{min}}$ can be considered to take into account the main source of error of the SfM-MVS-4D data. Terrain roughness affects the ability of the SfM-MVS algorithm to reconstruct the dense point cloud, since the error due to roughness depends on the position of the scan, which is never the same for multi-date missions, as well as the nature and occupancy of the terrain. We recall that vegetation is absent on our study gullies. This facilitates the calculation of roughness.

Then we also generated the interpolation error from a simple absolute difference between the altitude of the TIN node and the DTM-SfM Z_{DTM} $Z_{NodesTIN}$. Finally, for the error variable of the 3D point clouds we used the results of cross-validation.

The matrix data of the different variables were reclassified into four classes ('low', 'medium', 'high' and 'extreme') (Table 2).

Table 2. A four input fuzzy inference system for elevation uncertainty.

| Rule | Input | | | | Output |
|------|-----------|-------------------------------------|-------------------|-------------------------|---------------------------|
| | Slope (%) | Point Density (Pts/m ²) | 3-D Point Quality | Interpolation Error (m) | Elevation Uncertainty (m) |
| 1 | Low | Low | NA | NA | High |
| 2 | Low | Medium | NA | NA | Medium |
| 3 | Low | High | NA | NA | Low |
| 4 | Medium | Low | NA | NA | High |
| 5 | Medium | Medium | NA | NA | Medium |
| 6 | Medium | High | NA | NA | Low |
| 7 | High | Low | NA | NA | High |
| 8 | High | Medium | NA | NA | High |
| 9 | High | High | NA | NA | Medium |
| 10 | Extreme | NA | NA | NA | Extreme |
| 11 | NA | NA | High | High | Extreme |

2.5. Geomorphic Change Detection

An error model makes it possible to associate the control measurements made in the field with an accuracy estimate (example standard deviation in X, Y and Z). When applying the SfM-MVS method to create a digital terrain model, the errors generated are related to several factors such as the position and precision of the control points, camera distortions, resolution, number of photos, processing software, topographic complexity, interpolation methods, surface humidity, vegetation, etc., [38–40]. Several sources of error also affect the quality of DTMs for LiDAR data. These sources of error include terrain complexity, vegetation, weather, variation in point density, data filtering process and interpolation technique [41].

2.5.1. DEM of Difference (DoD)

This approach measures the vertical distance between two DEMs, through a simple subtraction between the pixels of these two DEMs according to the Equation (2). But before calculating the difference between the DEMs, a threshold value must be set for the minLoD (Equation (2)) [42,43]. This threshold means that subtraction values lower than minLoD are revealed as being uncertainties of the two numerical models. We can thus assign a value for the minLoD with confidence intervals that we can set. The user must define this threshold (statistic) according to the probability that he wishes to have so that the detection of changes can be real (Equation (2)) [44]. This fast method allows to determine the uncertainties related to the roughness of the terrain, the quality of the point clouds and the acquisition of the point clouds. However, great uncertainty in the quantification of sediment budgets occurs when the DEMs are not precise (since the minLoD threshold will be higher).

$$\text{minLoD} = \sqrt{\varepsilon_{2i}^2 + \varepsilon_{1i}^2} \text{ or } \text{minLoD} = t\sqrt{\varepsilon_{2i}^2 + \varepsilon_{1i}^2}; \quad (1)$$

where

- $t = \frac{Z_{2i} - Z_{1i}}{\sqrt{\varepsilon_{2i}^2 + \varepsilon_{1i}^2}}$
- ε_1 = The individual error of pixel i of first DTM
- ε_2 = The individual error of pixel i of second DTM
- t = is the critical value for a given confidence interval (1.28 for 80% CI, 1.96 for 95% CI); and
- z_2 and z_1 are the elevations in a given cell of DEMs.

2.5.2. Multi-scale Model to Model Cloud Comparison-Precision Maps (M3C2-PM)

M3C2-PM is an integrated approach in the CloudCompare software. It is used to directly compare dense point clouds in 3D instead of comparing DTMs or Mesh. The technique calculates the distance in the best perpendicular direction to the surface, with a confidence interval normally set at 95% (to assess the statistical significance of small topographic changes) and a measurement accuracy estimated from the point cloud roughness, allowing us to detect real topographic changes in elevation and planimetry between two degraded surfaces by gullying (erosion or sedimentation). The combination of three factors makes this the preferred method for determining the uncertainty of our digital terrain models: It can work perfectly even with changes in point density and even in the case of missing data. It calculates the distance between point clouds along the normal direction of the surface (the calculation of uncertainty on quasi-vertical areas). It estimates a spatially variable uncertainty for each point cloud and in accordance with terrain roughness and coregistration error [31,45]. To apply the M3C2 method, two parameters must be defined:

- 'D': Scale and orientation of the normal are used to calculate the normal area of each point which depends on the roughness and geometry of the point clouds. In the case of bank gullies we first applied a local model of <Quadratic >shape along the preferential axis to orient the reference point cloud towards the comparison point cloud. Then we chose the value of $D/2 = 10$ cm to look for neighbouring points in the reference point cloud while taking into account the terrain roughness.
- 'd': Projection scale, or the diameter of the cylinder in which the average distance of each surface of the point clouds is calculated. In this study we used a value of $d = 20$ cm.

3. Results

3.1. Data Processing

3.1.1. Data Precision

In this section we will focus mainly on the application and comparison of different error quantification techniques related to the collection and processing of SfM-MVS-4D data. Working on gullies of complex topography, the quantification of errors related to SfM-MVS data along three types of bank gullies allows on the one hand to analyze the reliability of the methodology adopted for data collection, and on the other hand to quantify with great precision the sediment budget over a relatively wet year.

Georeferencing Errors

The mean uncertainty values of the GCPs in XYZ were 1.5 cm (X), 2.4 cm (Y) and 5 cm (Z) (Table 3). These DGPS data processing results highlighted a flaw in the methodology for collecting GCP point's network. The points installed at the bottom of the gullies have a low accuracy compared to the others. They don't exceed 4 cm at best. This can be explained by the poor reception of the GNSS signal at the bottom of the gullies. The low precision of certain points reduced the general network precision of the GCPs, but this accuracy of the GCPs does not call into question the precision of the results since the three study sites were covered by a network of photos of high geometry that testify, by the total absence of systematic errors, to the shape of the surfaces such as the appearance of domes. In our case study, to georeference a network of photos with a high overlap, we used a network of GCPs well distributed spatially but of low precision. This greatly improved the georeferencing of the point clouds, where the value of the mean vertical RMES XY error is less than 2 cm for the 1st and 2nd sites and does not exceed 1.3 cm for the third (Table 3). The reprocessing of the geometry of the aerial photo network, either using a high rate of overlap, or with the combination of two modes of oblique and nadir acquisition, allowed us to obtain very precise internal measurements but weakly georeferenced in the external coordinate system.

Since the GCPs placed at the bottom of the gullies caused a degradation in the quality of their point network, it is necessary to ensure that the error in the SfM-MVS-4D results is acceptable.

Table 3. Errors in X, Y and Z of the three sites.

| Sites | B.G-1 | | | B.G-2 | | | B.G-3 | | |
|--------|-------|------|-------|-------|-------|-------|-------|------|-------|
| | M-I | M-II | M-III | M-I | M- II | M-III | M-I | M-II | M-III |
| X (cm) | 1.93 | 2.96 | 2.17 | 3.26 | 4.94 | 4.47 | 1.46 | 1.01 | 1.18 |
| Y (cm) | 2.19 | 3.13 | 2.37 | 3.36 | 4.53 | 4.46 | 1.27 | 1.60 | 1.82 |
| Z (cm) | 5.32 | 5.13 | 4.87 | 5.3 | 5.79 | 5.67 | 1.36 | 1.44 | 1.98 |

Accuracy analysis of the control points showed a strong degradation in the accuracy of the control points depending on the depths of the gullies. This is due to the poor reception of the GNSS signal at the bottom of the gullies, which led us not to use GCPs for point cloud validation. In this study we chose to evaluate the quality of the data by three methods.

The Uncertainty of Coregistration

We presented in the methodology the procedure used for the coregistration of dense point clouds using the ICP algorithm which allows to considerably increase the accuracy of georeferencing of SfM-MVS-4D data in an external georeferencing system. One of the main sources of error in detecting changes between two point clouds is uncertainty in coregistration. Even with low coregistration uncertainties between each pair of dense point clouds, the risk of the uncertainty amplifying increases with the temporal resolution of the point cloud collection. To reduce the risk, we proceeded by coregistration in pairs of point clouds. Here we seek to assess the quality of dense point clouds from a dual coregistration (GCP and ICP). Data uncertainty is modeled using three spatially variable models: FIS and cross-validation.

Cross Validation

The training and validation data are constructed by resampling without replacement, which allows us to calculate the uncertainty on the different cloud points. This method is more robust, more stable and more thorough than Bootstrapping (resampling with discount). To our knowledge, this method has never been used to quantify the uncertainty of point clouds. The quantification of the uncertainty of the point clouds with the cross validation tools was successfully carried out for the three bank gullies. Analysis of the uncertainty results obtained by the cross-validation method shows that the absolute difference can go up to 0.5 m, but the frequency distribution shows an dissymmetry with an absolute average for the three gullies not exceeding 0.08 m and a standard deviation of 0.09. The repetitive analysis of uncertainty on the three gullies has brought to light aspects of the spatial structure of uncertainty. The visual interpretation of the results (Figure 9) aimed that the high uncertainty values tend to be concentrated on the talwegs (main and secondary), and on some parts of the slopes. On the other hand, the low values are generally found in the flat areas and at the tops of the gullies. The uncertainty values are plotted against the slope and the roughness. On the Figure 9, it appears that all the high values of uncertainties are strongly correlated with the steep slopes and the zones of strong roughness what met in relation to the spatial distribution of the uncertainties with the topographic complexity and the roughness of ground. It must be concluded that roughness and slope are the main sources of errors. In several studies carried out, in order to determine the accuracy of the SfM-MVS data, the DGPS surveys of the GCPs are compared with the final product (DEM-SfM-MVS). This confusion is deliberately maintained, as if the uncertainty of the SfM-MVS data was only related to the quality of the DGPS surveys, and that the geometry of the photos taken could not improve the accuracy of the data. In our case of river gullies, the possibility of using a high number of photos, of high overlap, of including oblique photos as well as the double coregistration of point clouds with the ICP algorithm allowed us to compensate and to improve the georeferencing weaknesses by the GCPs.

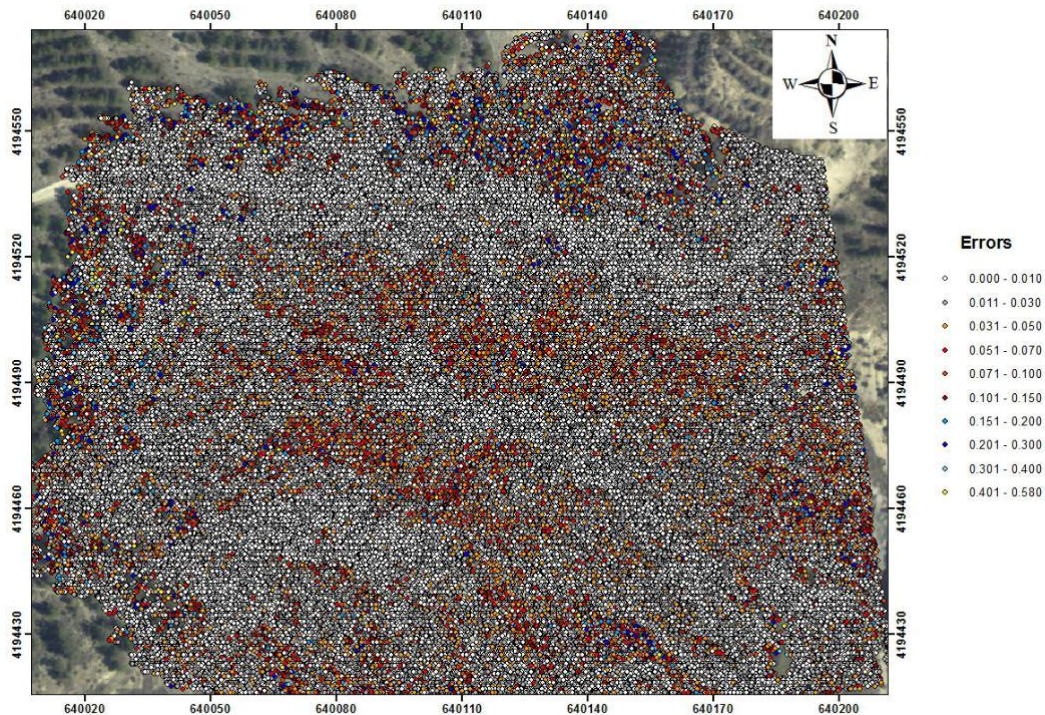


Figure 9. Example of point cloud uncertainty estimated by cross-validation on the gully B.G-1.

FIS

The results of the detection of geomorphological changes by the DoD technique are influenced by the type of error model used (spatially uniform or variable). Spatially uniform models can lead to overestimation or underestimates of topographic changes.

The FIS model, on the other hand, allows the changes to be reflected thanks to its better resolution, which leads to a better interpretation of the results. This is due to its ability to exclude noise, which is more important than for other models, also it leaves a morphological signature. Finally the results are transcribed in the form of a histogram, often bimodal. This tool facilitates the quantification of real changes in topographic models.

For the current study, on the three bank gullies, we detected geomorphological changes in the gullies with spatially variable FIS models. As the resolution of the data influences the detection of changes, we chose to use this model with a resolution of 5 cm. This technique allowed us to detect all possible changes, even the smallest ones, for our digital terrain models.

3.2. Detection of Geomorphological Changes from UAV Data

All change detection measurements over a period of time represent the result of the aggregation of all geomorphological processes. Positive values are assigned to all sedimentation processes, while negative values are appropriate for all erosion processes. According to the change map established by the DoD technique and the FIS propagated error, on both sides of the B.G-1 gully, erosion occurs with a significant difference between the two. This difference is mainly due to the exposure of the two slopes. The results of the two change detection techniques are similar but differ slightly in the quantification of sediment budgets. This small difference corresponds to the error model used by each technique. The two change detections are implemented by spatially variable error models. M3C2 uses roughness and coregistration error as error model variables. The FIS combines all the potential sources of errors (slope, point density, interpolation error, DTM-SfM-MVS error) to obtain a single error model. However, it is possible that the M3C2 technique underestimates the SfM-MVS error model.

3.2.1. DOD in Site 1

In general, monitoring of the sediment balance on the bank gully (B.G-1) allows us to notice significant changes during the year 2018. The bank gully (B.G-1) is located 250 m from the reservoir with a V shape.

Upstream the B.G-1 gully is covered by tree strata forming a protective layer. In this area of the gully, the changes are not significant, but photo-interpretation of the PNOA orthophotographs shows a strong degradation of the vegetation cover due to the digging of the head of the gully. The orthophotographs generated by the SfM-MVS data showed significant immobilization of the wood planks on the gully bed (Figure 10). On the south-western south facing slope, the annual rate of erosion between the 1st and 3rd missions varied between 30 and 60 cm/year with vertical erosion. Conversely, a low erosion rate of no more than 10 cm/year was recorded on the north-northeast facing slope. However, the rate of erosion is not constant on the same slope. That said, the rate of erosion or sedimentation varies according to the slope, roughness, and exposure of each slope (Figure 10).

It should be noted that the sediment balance on the gully (B.G-1) during the wet season shows a dominance of erosion activity over the entire gully. The south-western south slope shows the highest erosion rates of the gully. On the other hand, there are spatial variations in the erosion rate within the same slope, highlighting the contrast in the existence of land use variation upstream of the gully.

On the gully bed this dynamic is reversed. The transfer of sediment to the bed has generated a fattening of the bed. Between the first and the third mission, the calculated sedimentation rate is of the order of 353.85 T/ha/year ($442.31 \text{ m}^3/\text{ha}/\text{year}$) (Figure 10) which does not reach the reservoir.

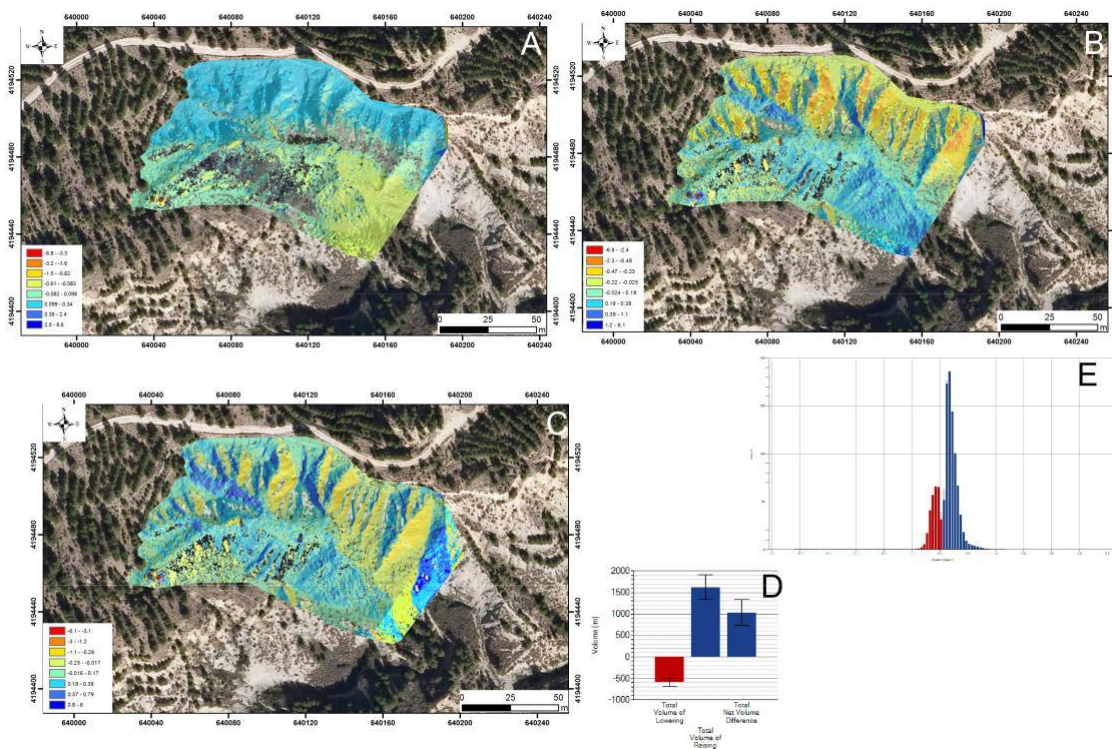


Figure 10. Bank gully (B.G-1)(A) DoD Mission I and II. (B) DoD Mission II and III. (C) DoD Mission I and III. (D) Graph of DoD volume. (E) Bar chart of DoD volume change distribution (erosion volume in red, deposition volume in blue).

3.2.2. DOD in Site 2

The U-shaped B.G-2 gully, located near the reservoir, is highly exposed to erosion. The results measured by the DoD method have further highlighted the variation in the erosion rate between the two sides of the gully. The results show a strong activity of the annual sedimentation rate on the

north-facing slope as opposed to the south-facing slope where the annual erosion rate exceeds 90 cm of digging. Similarly, on the map, we observe significant changes at the head of the gully. These changes are reflected by an erosion rate of up to 2 m/year (Figure 11).

On the gully bed we observe the same sedimentation phenomenon as in Gully B.G-1 since this sector represents a sedimentary basin of the elements eroded by the banks and the head of the gully. The results of the DoD method show that the annual sedimentation rate at the bottom of the gully is of the order of 4264.1 T/ha/year ($5330.1 \text{ m}^3/\text{ha}/\text{year}$) (Figure 11D). At the time of maximum filling of the lake the bottom of the gully corresponds to the bottom of the lake.

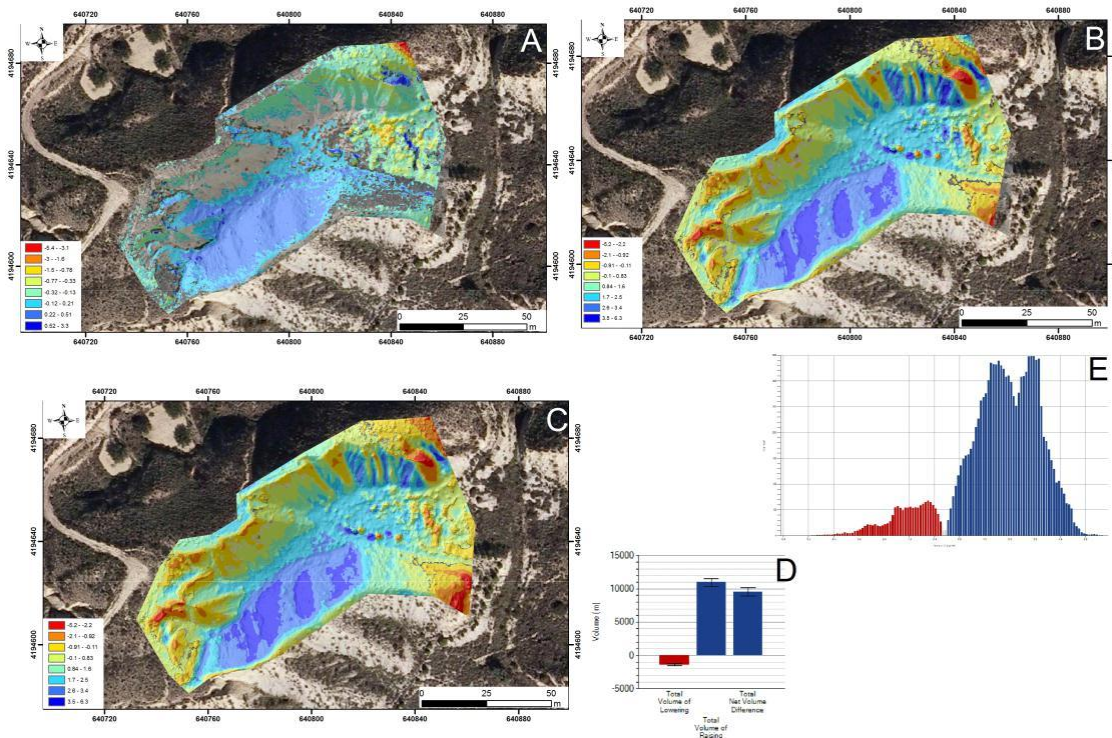


Figure 11. Bank gully (B.G-2)(A) DoD Mission I and II. (B) DoD Mission II and III. (C) DoD Mission I and III. (D) Graphe of DoD volume. (E) Bar chart of DoD volume change distribution (erosion volume in red, deposition volume in blue).

3.2.3. DOD in Site 3

For the gully (B.G-3), the result of the sediment balance reveals that the rate of erosion is slightly lower than the rate of accumulation during the wet season. This is because the water level decreased by 1 m between the first and second field missions, which limits the sediment transport capacity by littoral drift and waves, but also that, in its bed, the gully experienced a strong sedimentation activity after the mixing of the lake water (regression deposits). Thus, during this season, the lakeshores were less watered. The sedimentation rate is the highest on all the slopes. The volume of sediment decreases from upstream to downstream of the gully bed. During the dry season, the banks were watered more, resulting in a high erosive potential (Figure 4) and a higher rate of slope erosion, estimated at 1772 m^3 . Thus, the dry season of 2018 contributed to the triggering of the gully process after episodes of heavy rainfall. The particles eroded on the slopes are transported by the water to the gully bed and the lake. The rate of sediment accumulated in the gully bed is 1993 m^3 . The sedimentation rate of the gully (B.G-3) is estimated at 138.3 T/ha/year ($172.7 \text{ m}^3/\text{ha}/\text{year}$) (Figure 12).

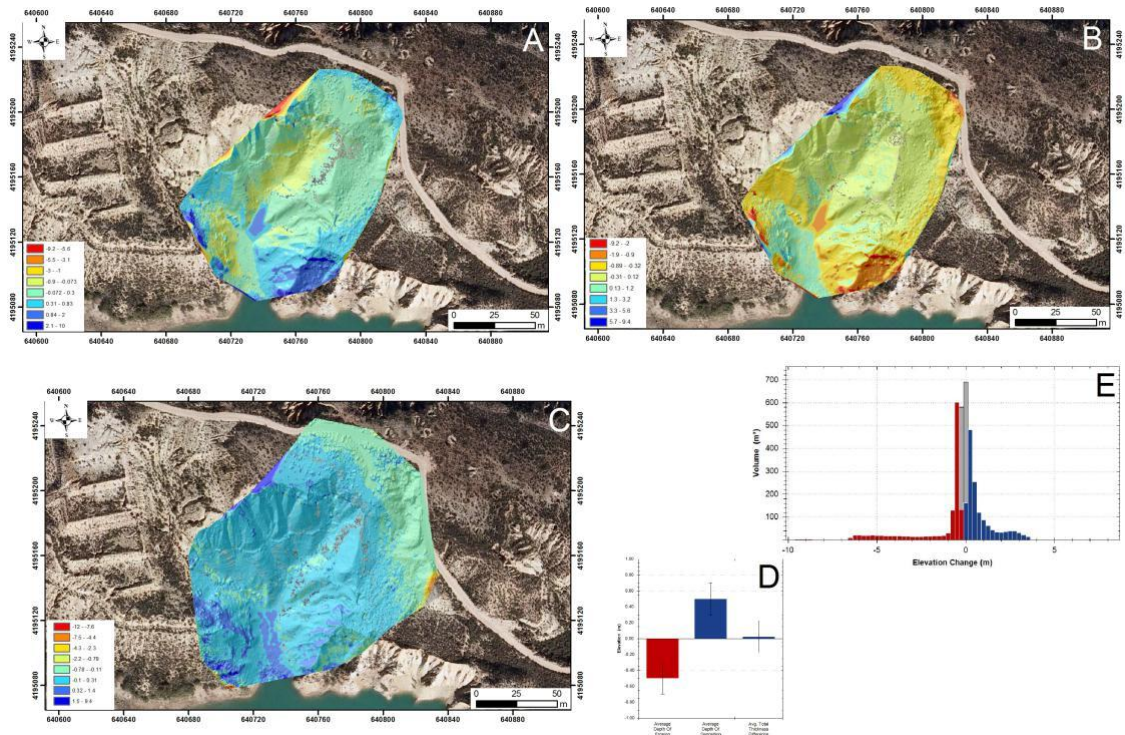


Figure 12. Bank gully (B.G-3)(A) DoD Mission I and II. (B) DoD Mission II and III. (C) DoD Mission I and III. (D) Graph of DoD volume. (E) Bar chart of DoD volume change distribution (erosion volume in red, deposition volume in blue).

3.2.4. M3C2 in Site 3

The Gully (B.G-3) is formed by overhanging slopes. To quantify the sedimentation rate of this particular morphology we used a 3D comparison of the point clouds using the M3C2 algorithm, in order to take into account the share of sediments coming from the overhanging areas. This method seems to us more complete than the DoD method, which allowed us to highlight the difference between 2.5 D digital terrain models. This gully is typical of heterogeneous soil formations rich in clay. It is developed on the concave bank of the Rambla de Algeciras where the reservoir constitutes a sedimentary basin of products from the eroded slopes of the gully. The gully (B.G-3) is the result of a combined erosion of the slopes and tunnels. This complex shape is representative of the fragile geomorphological bank gullies. The tunnels formed on Gully B.G-3 are related to the high clay contents in the upper soil horizon (river deposits). In this part of the gully the water carries away the clays and forms tunnels that develop until the ground collapses. From this we can deduce several results about the erosion rate illustrated in particular by distance measurements. Concerning the tunnel zones, the changes are almost zero. It appears that they remain stable, but these areas are very dangerous because their evolution is unpredictable. At the bottom of the gully, the sedimentation rate is very high, exceeding 250 m^3 over an area of 2.28 ha. We notice that the erosion rate on both sides of the gully is similar, which seems logical for an area with steep slopes and no vegetation cover. It is clear from the distance measurements that the sedimentation rate at the bed of gully B.G-3 is higher than for the other gullies.

3.3. Detection of Geomorphological Changes from LiDAR-PNOA Data

The Figure 13 shows DoD values for all bank gullies along the lakeshore between 2009 and 2016. The value (minLOD = 0.28 m) was determined according to the equation (Equation 2). According to the gross DoD, about 45% of the lakeshore area has been gully eroded and the rest of the area has been

sedimented. The histogram (Figure 14B) of the distribution of elevation changes in the figure reflects the positive bias of the eroded areas.

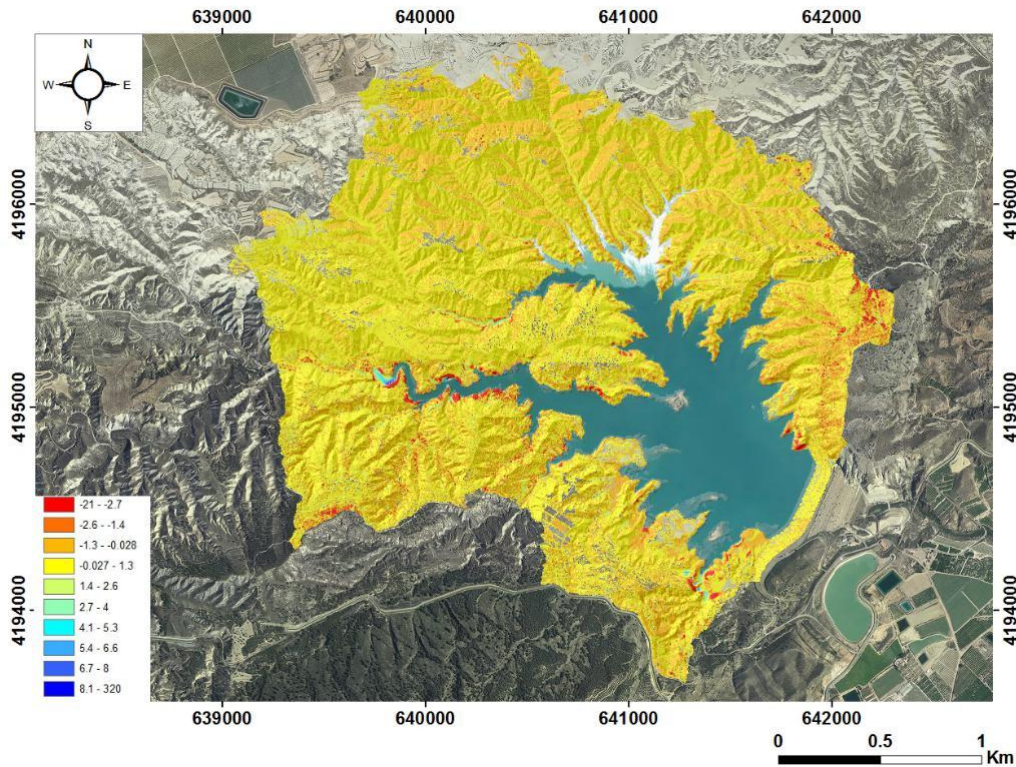


Figure 13. DoD in the lakeshore area for the survey PNOA 2009 and PNOA 2016.

Interpretations of the signature of topographic changes can be justified, however, taking into account the volume and area of the areas that have changed. The histogram (Figure 14A) shows that the total surface of the gullies undergoes changes in altitude due to erosion. On the histogram, we can visualize an imbalance between the rate of sedimentation and erosion on the lakeshore. This unbalanced sediment balance is represented by the asymmetric distribution of the elevation values around the value 0 with an erosion bias. Visualization of the histogram of the distribution of eroded or sedimented volumes on the lakeshore provides a more detailed view of the quantity of sediment deposited in the lake: between 2009 and 2016, 177,641 m³ (39 T/ha/year) of sediment was deposited (Figure 14A).

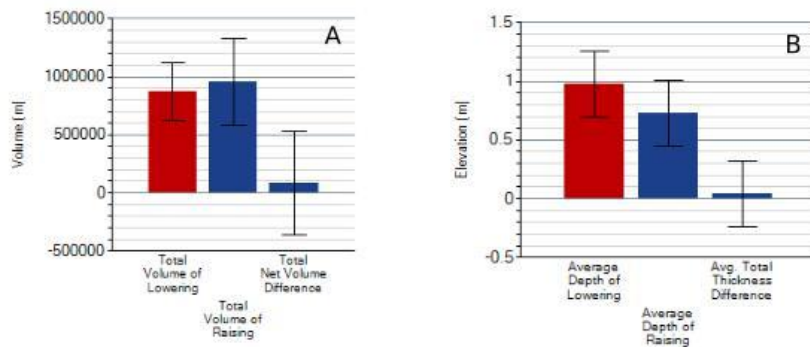


Figure 14. (A) Bar chart of DoD volume change distribution. (B) Bar chart of DoD elevation change distribution.

From the histogram (Figure 15), it can be seen that the highest morphological changes are in the eroded part with moderate concentrations but with a large amplitude reaching 0.98 m over a surface area of 900,000 m². The peak of the changes is not quite in the same area. This peak corresponds to a dominance of low amplitude accumulation processes of 0.7 m over an area of 1,300,000 m².

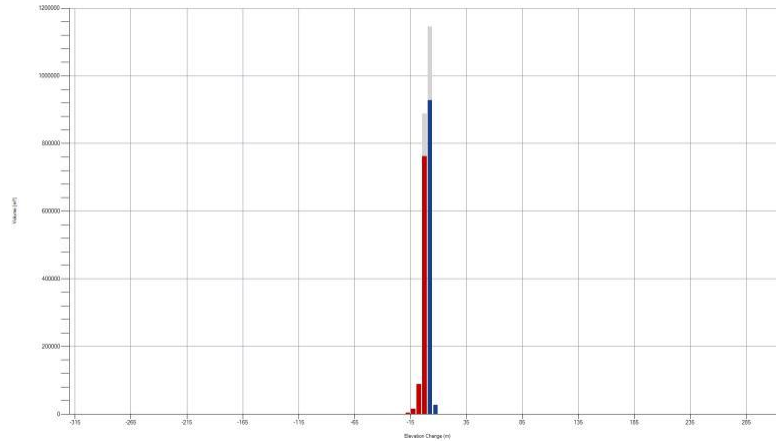


Figure 15. Histogram of elevation distribution.

From the multimodal distribution of the histogram (Figure 15), it is easy to conclude the complexity of the morphodynamic events of the embankment gullies, especially since the significant temporal variability of the R-factor agrees on this point.

With the LiDAR PNOA data two sediment budgets were established. The first calculated balance is really the result of the mean RMSEZ error of 0.2 m. The second is inherent to the actual cubic content of the balance with statistical thresholds that vary little. The results of these two balances vary slightly at the gully scale, but on all lakeshores the difference between the results of these two balances is significant.

4. Discussion

4.1. Data Acquisition

The acquisitions of SfM-MVS-4D data by UAV met our needs in terms of accuracy, and frequency of monitoring the gullies along the lakeshore. Throughout the shooting, the flight altitude remained at a quasi-constant level at each site during the three missions, allowing us to keep the same pixel resolution for each gully. The UAV flew over the gullies at an altitude varying between 28 and 37 m, which allowed us to guarantee adequate resolution for monitoring topographic changes in the gullies. We also noted that the choice of these altitudes allowed us to ensure a small B/h ratio of the order of 0.6, in order to minimize as much as possible the surface of the hidden areas.

The results of the dense point clouds obtained by a vertical shot provide significant information on the topography of the gullies (B.G-1 & 2) compared to the gully (B.G-3). However, it should be noted that the photos taken on the gully (B.G-3) with a vertical camera do not cover the entire studied area. The overhang, having a vertical geometry, could not be taken into consideration. Moreover, the photos taken with an oblique camera were very useful to link the base and the top of the gully overhang slopes. Several previous studies have shown that the systematic errors of the dome effect significantly decrease or even eliminate after the use of an oblique and nadir image acquisition configuration, regardless of the image overlap rate, the camera angle and the configuration of the oblique and nadir images [46,47]. On the gullies (B.G-1 and B.G-2) the aerial photos are taken at nadir. The application of the integrated approach of the two flight configurations, i.e. nadir (90°) and oblique (30°) acquisition, reinforces the geometry of the photo network on the gully (B.G-3). This technique of oblique photo

acquisition increases the overlap rate between the photos, making it possible on the one hand to densify the density of the point clouds and on the other hand to fill the void created by the topographical complexity of the gullies (overhang). This therefore reduces georeferencing errors linked mainly to the low precision of the GCPs. We noted that the integrated approach has considerably reduced the RMSE in XYZ of the GCPs on the gully (B.G-3) with an average that does not exceed 1.4 cm in X, 1.2 cm in Y and 1.3 cm in Z during the three missions, bearing in mind that the GCPs went from 16 points to 12 points during the last mission. For the gullies (B.G-1; 2) it is the opposite, since the RMSE errors are high and vary between 2 and 5 cm.

4.2. Data Processing

Vertical and oblique photos are somewhat contrasting since the angle between the two shooting modes fluctuates very strongly along the same swath. Alignment in the PhotoScan software of the photos from two angles failed. The alignment results of the two shooting modes contain only the sparse point cloud from the nadir photos. To solve this problem we realigned all the photos using the common GCPs on both photos and the geolocation data of the photos before applying the bundle adjustment model.

Then we included the following camera parameters: Fit F, Cx, Cy, K1, K2, K3, P1, P2 (Table 4) which improved the camera model and reduced the RMSE errors of the photos as well as the deviations at the GCP point networks. The parameters were selected based on correlation analysis where high correlation parameters were eliminated to avoid over-configuration of the camera model. In this case study Mean precision across the camera is 0.10, this precision value will allow us to evaluate the correlation between the camera parameters. The low correlation between the parameters indicates a good image network except for the radial parameters, however when the correlation between F and Cy is very high this is explained by the absence of large camera rotation and a slight weakness of the image network. In our case study, the value is very close to the accuracy which illustrates the good image network taken in the field.

Table 4. Correlation between the camera parameters.

| | F | Cx | Cy | K1 | K2 | K3 | P1 | P2 |
|----|----------|-------------|-------------|-----------|-------------|-------------|-------------|-------------|
| F | 1 | 0.61 | 0.13 | 0.07 | 0.06 | 0.08 | 0.51 | 0.22 |
| Cx | | 1 | 0.04 | 0.05 | 0.8 | 0.06 | 0.33 | 0.03 |
| Cy | | | 1 | 0.01 | 0.02 | 0.02 | 0.17 | 0.76 |
| K1 | | | | 1 | 0.80 | 0.90 | 0.03 | 0.02 |
| K2 | | | | | 1 | 0.89 | 0.02 | 0.00 |
| K3 | | | | | | 1 | 0.00 | 0.01 |
| P1 | | | | | | | 1 | 0.17 |
| P2 | | | | | | | | 1 |

4.3. Error Modeling

We took advantage of the Lidar PNOA data collected between 2009 and 2016 to continue the analysis of the morpho-sedimentary dynamics of the three gullies. Similarly, the work was enriched by taking into account the spatio-temporal variability of the dynamics of all the bank gullies as a function of topographical influence and climate action. We present and analyze here the results of the raw DoD method obtained from the difference between the two DEMs Lidar 2009 and 2016 of the PNOA project. however, the error of the two Lidar missions PNOA 2009 and 2016 is of the order of 0.28 m this value is considered spatially homogeneous and uniform for two main reasons:

(1) The low density of the Lidar point clouds (between 0.5 and $1/m^2$): the denser the point cloud is, the more robust it is to accurately determine terrain parameters such as slope or roughness.

(2) The absence of GCPs: the georeferencing errors of the GCPs are essential to estimate an error model of the Lidar PNOA data.

To quantify the uncertainty of the SfM-MVS data accurately, it is necessary to validate the SfM-MVS data by a comparison with previous SfM-MVS data or with a very high precision field truth (DGPS, TS). The method of validation is often dictated by the extent, scale, field survey method, data format, and morphological characteristics of the study site.

In this paper we first chose to quantify spatially variable SfM DEM uncertainty, using the cross-validation method instead of Bootstrapping which has already been used by Wheaton and [35] and Rossi [48]. Then the uncertainty values will be used to build an error model that takes into account the different sources of uncertainty using the FIS model.

Several works have shown that the vertical accuracy on the GCPs control points is about two to three times higher than the accuracy obtained by the products derived from the SfM-MVS data (DTM and orthophotography) [49,50]. The table (Table 5) shows that the FIS error propagation model estimates higher vertical errors on GCPs points than those obtained after georeferencing (Table 3). The accuracy of the SfM-MVS data obtained during this study is comparable to that of the GNSS/TS data [35,51].

Table 5. FIS errors in X, Y and Z of the GCPs.

| Sites | B.G-1 | | | B.G-2 | | | B.G-3 | | |
|----------|-------|-------|-------|-------|-------|-------|-------|------|-------|
| Missions | M-I | M-II | M-III | M-I | M- II | M-III | M-I | M-II | M-III |
| X (cm) | 3.62 | 3.63 | 4.02 | 6.21 | 6.33 | 6.52 | 2.63 | 2.21 | 2.54 |
| Y (cm) | 4.45 | 6.12 | 3.24 | 4.06 | 6.87 | 6.77 | 2.31 | 3.12 | 3.05 |
| Z (cm) | 10.53 | 12.69 | 9.35 | 11.55 | 12.81 | 11.31 | 2.80 | 3.32 | 3.54 |

4.4. Detection of Geomorphological Changes

From the Figure 16 we observe a ramified gully system on the entire lakeshore, with a gully density varying between 18 km/km^2 and 59 km/km^2 with an annual erosion rate of 39 T/ha/year these values are extreme are of the same order as some areas that reach values varying between 15% and 60% [52–55].

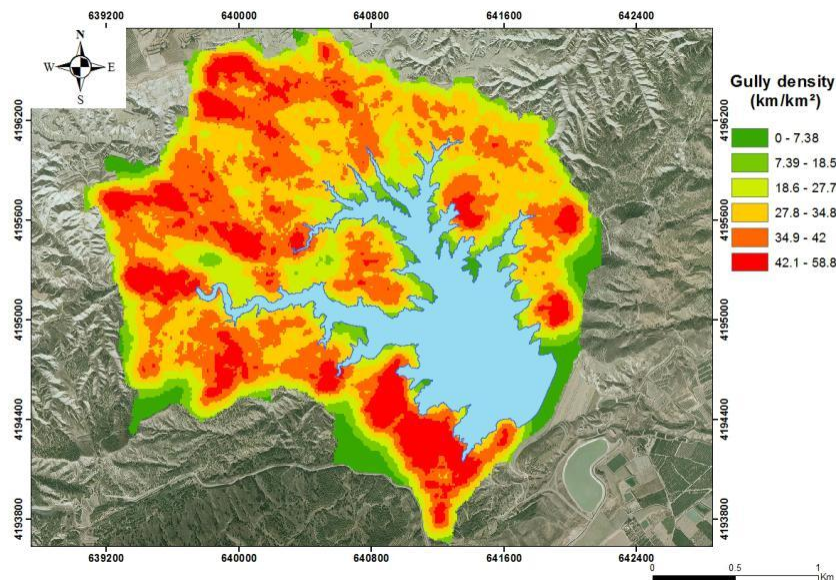


Figure 16. Bank gullies density.

Globally, the volume eroded by gullies varies between 0.002 and $47,430 \text{ m}^3/\text{year}$ with an average of $358.6 \text{ m}^3/\text{year}$. In the Murcia region, research on the gully erosion is limited. As a result, there is very little data on the gully erosion budget. Indeed, in the literature, we find two references on the sediment balance of gullies and bank gullies in the Guadalentin watershed downstream of the

Rambla de Algeciras watershed, namely the work of L. Vandekerckhove [56] and Marzloff [57]. Before comparing the results of this study with those of Vandekerckhove and Marzloff, it should be pointed out that the very complex morphology, the very friable pedology and the strong anthropic activity in the Rambla de Algeciras catchment area allowed us to consider that the Guadalentin basin is less vulnerable to gully erosion than the Rambla de Algeciras basin. Despite this observation, the volumes calculated in this work are close to the results estimated in this study. The annual volume calculated by Vandekerckhove over some time varies between 40 and 43 years based on aerial photos and field measurements vary between 13 and 3467 m³/year. Similarly, Marzloff's work in 2011 using aerial photos taken by the UAV showed that the rate varies between 0.5 and 100 m³/year. On the gully (B.G-3) we have estimated the volume eroded from the calculation of the distance between the 3D SfM-MVS point clouds according to the direction of the surface normals, rather than the difference between two 2.5 D rasters. This technique takes into account the volume of sediments eroded on the gully overhang area. The M3C2 algorithm calculates the distance between the multi-temporal point clouds, which allows to estimate the eroded volume with high accuracy. The results of the M3C2 technique thus testify on the good choice of an oblique and nadir acquisition configuration on the gully (B.G-3) to generate accurate and complete SfM-MVS data.

The analysis of the geomorphological changes estimated by the UAV and LiDAR are very different, with the results of the LiDAR data the percentage of the eroded area over the whole period 2009–2016 is not more than (45%) however the deposit areas are more important with a percentage of (55%). On the other hand, the estimates of the sedimentary balance during the year 2018 with the UAV data allow us to observe an erosion activity that affected on average more than 60% of the surface of the studied gullies. The results of the LiDAR data appeared aberrant but the monitoring of the fluctuation of the lake level explains the strong sedimentation activity on the lake banks between 2009 and 2016. The rise of lake level is related to the high trend in rainfall inputs between 2010 and 2015 (Figure 17). It should also be noted that the lake level decreased from 260 m in 2014 to 240 m in 2018. This is related to the decrease in rainfall inputs between 2015 and 2017. This water level fluctuation has caused the settling of regression deposits. After the period of maximum lake filling at 260.12 m (4 May 2014), the lakeshore has experienced silt sedimentation in flat areas and gully beds. These sediments have four origins:

- Gullying (Figure 18)
- Bluff slumping (Figure19)
- Biogenic (biological activity)
- Detritic (torrential inputs of Rambla)

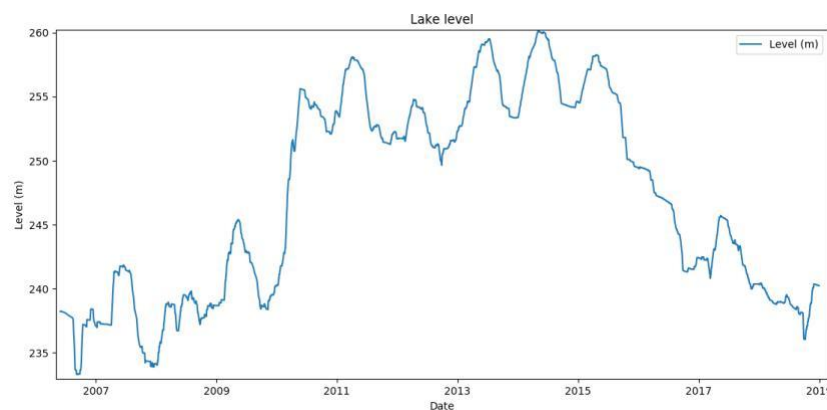


Figure 17. Lake level fluctuation between 2006 and 2019.

The photo-interpretation of PNOA orthophotography illustrates an imbalance in the morphodynamics of the lakeshore.

When the lake level reached the rills and small gullies, the vertical movement of the lake water overwhelmed them and caused them to lose their erosion ability (Figure 18). This has led to the temporal disappearance of these small forms of erosion. They were then replaced by the sedimentary activity of waves loaded with suspended matter (a process linked to longshore drift).

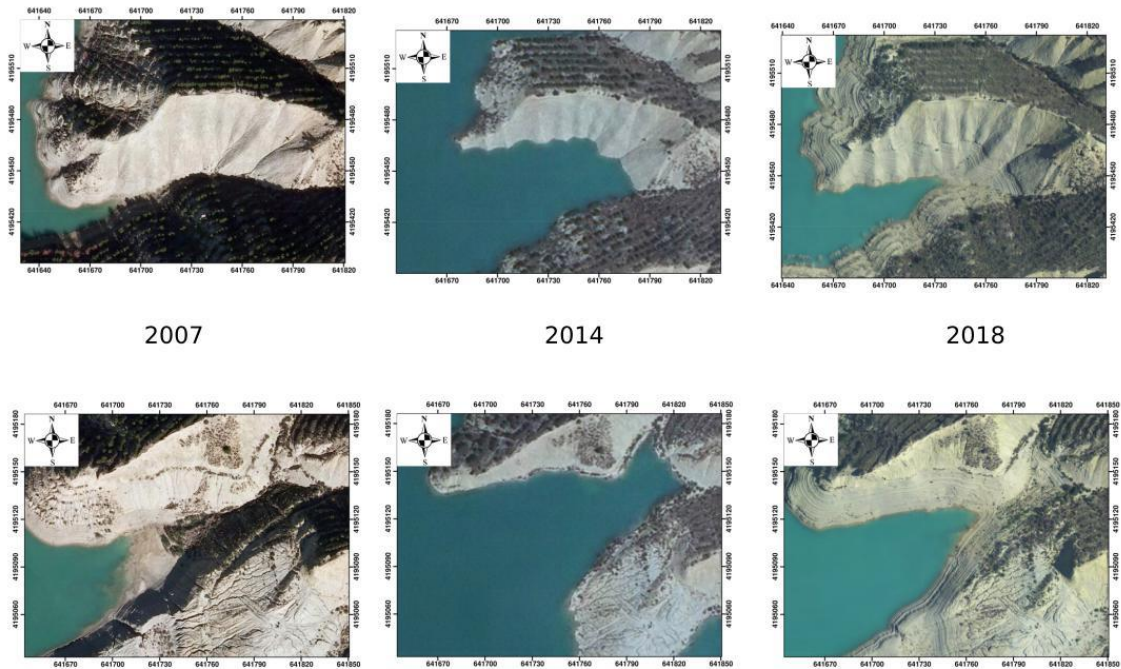


Figure 18. Temporal disappearance of the small bank gullies.

The missing data on the solid transport at gauging stations tributaries of the Rambla, prevent from quantifying the sediment inputs into the Rambla de Algeciras, as it has been done in Morocco by Ezzaoui et al [58], and unfortunately also, we have not been able to install sedimentimetres [59] in the lake to collect and analyze the nature and percentage of detrital and biogenic sediments, mainly due to time and money issues.

The bluff slumping of the lakeshore, observed through photo-interpretation of the PNOA aerial orthophotographs between 2009 and 2016, is a phenomenon triggered during the maximum filling of the lake. The former overhanging areas are destabilized by moisture and weight. This phenomenon is localized in particular on the meanders and concave banks of the Rambla (Figure 19).

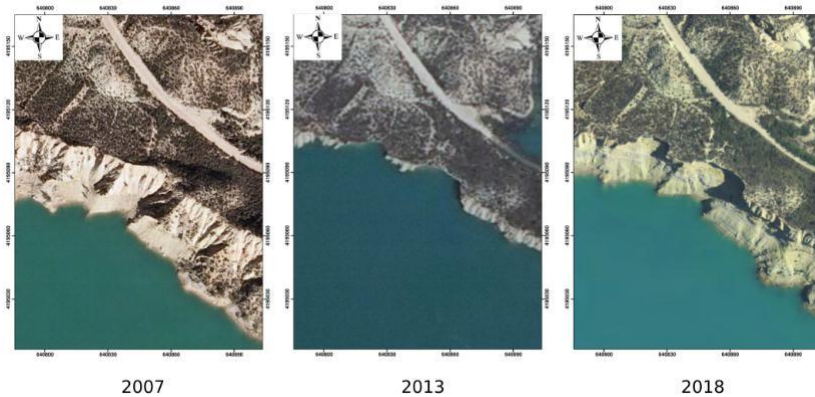


Figure 19. Bluff slumping.

5. Conclusions

The friable nature of the soil, the fluctuation of the lake level, anthropic activity and climate changes marked by increasingly rare but very violent rainfall episodes have made it possible to carve out several forms of gullies on the lakeshores of Rambla de Algeciras. The main goal of this paper is to demonstrate whether the SfM-MVS-4D model generated from photos taken by a UAV and the LiDAR PNOA data, are able to accurately quantify the sediment budget on the banks gullies of the lakeshores. The answer is yes. Indeed, for bank gully monitoring on lakeshores, we detected geomorphological changes on three types of banks gullies. The models for the detection of geomorphological changes were constructed using multi-temporal numerical terrain models coupled with spatially variable uncertainty models. The rate of geomorphological changes detected on the three gullies in 2018 is mainly related to orientation, land use and the shape of the gullies.

The aerial photos taken by the UAV are capable of generating SfM-MVS-4D models with very high spatial and temporal resolution, which allows to highlight the movement of sediments along the slopes of the gullies. The use of the nadir and oblique configuration for taking pictures has improved the accuracy of the SfM-MVS models taken on very steep slopes or with overhangs. This accuracy was measured using several techniques, namely georeferencing error estimation and the statistical cross-validation approach and finally the FIS technique. This was useful for detecting geomorphological changes on banks gullies. The accuracy of the SfM-MVS data varies between 1 and 5 cm.

The data from the PNOA project (orthophotographs and LiDAR) provided reliable and accurate data to study the effects of lake level fluctuation, climate change and land use change on the initiation of lake bank gullying. The DOD technique applied on the LiDAR data from the PNOA allowed the estimation of an annual sedimentation rate of 39 T/ha/year ($49 \text{ m}^3/\text{ha}/\text{year}$) from the gullies of the Rambla de Algeciras lakeshores.

We also note that the approach proposed in this paper will be deployed in Morocco on the Sidi Mohamed Ben Abdellah dam, which shares the same bank gully on lakeshores issues and geo-environmental characteristics as our study site.

Author Contributions: Conceptualization, V.M. and R.H.; Data curation, R.C.; Funding acquisition, R.C. and F.C.; Methodology, V.M., R.H. and F.C.; Project administration, G.M. and E.R.; Resources, V.M, E.R. and R.C.; Software, F.C.; Validation, R.H.; Writing—original draft, R.H.; Writing—review and editing, V.M, G.M. and R.H. All authors have read and agreed to the published version of the manuscript.

Funding: This research received no external funding.

Acknowledgments: This work has been financed with the following funds: GEOLAB laboratory and CASBA project and is gratefully acknowledged. The authors also want to thank Confederación Hidrográfica del Segura in Murcia, Mr Pablo Albaladejo and all colleagues, engineer and technicians participating in the field campaigns supporting successful data acquisition. Constructive and valuable feedback given from the anonymous reviewers helped to increase the quality of the paper.

Conflicts of Interest: The authors declare no conflict of interest.

References

1. Hentati, A.; Kawamura, A.; Amaguchi, H.; Nakagawa, N. Erosion assessment at small hillside river basins in semiarid region of Tunisia. *Annu. J. Hydraul. Eng. Jsce* **2010**, accepted under publication.
2. Antipolis, S. Les menaces sur les sols dans les pays méditerranéens (Etude bibliographique). *Les Cahiers du 690 Plan Bleu* **2003**, 2, 44–48.
3. Inoubli, N. Ruissellement et Érosion Hydrique en Milieu Méditerranéen Vertique: Approche Expérimentale et Modélisation. Ph.D. Thesis, Montpellier, SupAgro, Montpellier, France, 2016.
4. Castillo, C.; Gómez, J. A century of gully erosion research: Urgency, complexity and study approaches. *Earth-Sci. Rev.* **2016**, 160, 300–319.
5. Poesen, J.; Nachtergaele, J.; Verstraeten, G.; Valentin, C. Gully erosion and environmental change: importance and research needs. *Catena* **2003**, 50, 91–133.

6. Bull, L.J.; Kirkby, M.J. *Dryland Rivers: Hydrology and Geomorphology of Semi-Arid Channels*. John Wiley & Sons: Chichester, UK, 2002.
7. Vanmaercke, M.; Poesen, J.; Van Mele, B.; Demuzere, M.; Bruynseels, A.; Golosov, V.; Bezerra, J.F.R.; Bolysov, S.; Dvinskikh, A.; Frankl, A.; et al. How fast do gully headcuts retreat? *Earth-Sci. Rev.* **2016**, *154*, 336–355.
8. Nazari Samani, A.; Tavakoli Rad, F.; Azarakhshi, M.; Reza Rahdari, M.; Rodrigo-Comino, J. Assessment of the sustainability of the territories affected by gully head advancements through aerial photography and modeling estimations: A case study on Samal Watershed, Iran. *Sustainability* **2018**, *10*, 2909.
9. Valentin, C. *Les Sols au Coeur de la Zone Critique 5: D'Égradation et Réhabilitation*; ISTE Group: Santa Clara, CA, USA, 2018; Volume 5.
10. Wu, Y.; Cheng, H. Monitoring of gully erosion on the Loess Plateau of China using a global positioning system. *Catena* **2005**, *63*, 154–166.
11. Mockus, V. *National Engineering Handbook*; U.S. Soil Conservation Service: Washington, DC, USA, 1964; Volume 4.
12. Thompson, J.R. Quantitative effect of watershed variables on rate of gully-head advancement. *Trans. Asae* **1964**, *7*, 54-0055.
13. Seginer, I. Gully development and sediment yield. *J. Hydrol.* **1966**, *4*, 236–253.
14. Yuan, Y.; Bingner, R.; Rebich, R. Evaluation of AnnAGNPS on Mississippi delta MSEA watersheds. *Trans. Asae* **2001**, *44*, 1183.
15. Nachtergaele, J.; Poesen, J.; Vandekerckhove, L.; Oostwoud Wijdenes, D.; Roxo, M. Testing the ephemeral gully erosion model (EGEM) for two Mediterranean environments. *Earth Surf. Process. Landf. J. Br. Geomorphol. Res. Group* **2001**, *26*, 17–30.
16. Sidorchuk, A. Dynamic and static models of gully erosion. *Catena* **1999**, *37*, 401–414.
17. Tucker, G.; Lancaster, S.; Gasparini, N.; Bras, R. The channel-hillslope integrated landscape development model (CHILD). In *Landscape Erosion and Evolution Modeling*; Springer: Cham, Switzerland, 2001; pp. 349–388.
18. Evans, M.; Lindsay, J. High resolution quantification of gully erosion in upland peatlands at the landscape scale. *Earth Surf. Process. Landf.* **2010**, *35*, 876–886.
19. Maleval, V. *Les Apports Sédimentaires Directs au Barrage SMBA*; Workshop SIGMED, 2012. Available online: <https://hal-bnf.archives-ouvertes.fr/GEOLAB/hal-00924798v1/> (accessed on 29 September 2020).
20. D'Oleire Oltmanns, S.; Marzloff, I.; Peter, K.D.; Ries, J.B. Unmanned aerial vehicle (UAV) for monitoring soil erosion in Morocco. *Remote Sens.* **2012**, *4*, 3390–3416.
21. Castillo, C.; James, M.; Redel-Macías, M.; Pérez, R.; Gómez, J. SF3M software: 3-D photo-reconstruction for non-expert users and its application to a gully network. *Soil* **2015**, *1*, 583.
22. Wang, R.; Zhang, S.; Pu, L.; Yang, J.; Yang, C.; Chen, J.; Guan, C.; Wang, Q.; Chen, D.; Fu, B.; et al. Gully erosion mapping and monitoring at multiple scales based on multi-source remote sensing data of the Sancha River Catchment, Northeast China. *Isprs Int. J. Geo-Inf.* **2016**, *5*, 200.
23. Di Stefano, C.; Ferro, V.; Palmeri, V.; Pampalona, V.; Agnello, F. Testing the use of an image-based technique to measure gully erosion at Sparacia experimental area. *Hydrol. Process.* **2017**, *31*, 573–585.
24. Frankl, A.; Stal, C.; Abraha, A.; Nyssen, J.; Rieke-Zapp, D.; De Wulf, A.; Poesen, J. Detailed recording of gully morphology in 3D through image-based modelling. *Catena* **2015**, *127*, 92–101.
25. Christian, P.; Davis, J. Hillslope gully photogeomorphology using structure-from-motion. *Z. Geomorphol. Suppl. Issues* **2016**, *60*, 59–78.
26. Koci, J.; Jarihani, B.; Leon, J.X.; Sidle, R.C.; Wilkinson, S.N.; Bartley, R. Assessment of UAV and ground-based structure from motion with multi-view stereo photogrammetry in a gullied savanna catchment. *Isprs Int. J. Geo-Inf.* **2017**, *6*, 328.
27. Stocker, T.F.; Qin, D.; Plattner, G.K.; Tignor, M.; Allen, S.K.; Boschung, J.; Nauels, A.; Xia, Y.; Bex, V.; Midgley, P.M.; et al. *Climate change 2013: The physical science basis. Contrib. Work. Group Fifth Assess. Rep. Intergov. Panel Clim. Chang.* **2013**, 1535.
28. Zhang, Z. Iterative point matching for registration of free-form curves and surfaces. *Int. J. Comput. Vis.* **1994**, *13*, 119–152.
29. Stöcker, C.; Eltner, A.; Karrasch, P. Measuring gullies by synergetic application of UAV and close range photogrammetry—A case study from Andalusia, Spain. *Catena* **2015**, *132*, 1–11.

30. Micheletti, N.; Chandler, J.H.; Lane, S.N. Investigating the geomorphological potential of freely available and accessible structure-from-motion photogrammetry using a smartphone. *Earth Surf. Process. Landf.* **2015**, *40*, 473–486.
31. Lague, D.; Brodu, N.; Leroux, J. Accurate 3D comparison of complex topography with terrestrial laser scanner: Application to the Rangitikei canyon (NZ). *Isprs J. Photogramm. Remote. Sens.* **2013**, *82*, 10–26.
32. Mosbrucker, A.R.; Major, J.J.; Spicer, K.R.; Pitlick, J. Camera system considerations for geomorphic applications of SfM photogrammetry. *Earth Surf. Process. Landf.* **2017**, *42*, 969–986.
33. Cucchiaro, S.; Maset, E.; Fusiello, A.; Cazorzi, F. 4D-SfM photogrammetry for monitoring sediment dynamics in a debris-flow catchment: Software testing and results comparison. In Proceedings of the 2018 ISPRS TC II Mid-term Symposium “Towards Photogrammetry 2020”. International Society for Photogrammetry and Remote Sensing, Riva Del Garda, Italy, 4–7 June 2018; Volume 42, pp. 281–288.
34. Vericat, D.; Smith, M.; Brasington, J. Patterns of topographic change in sub-humid badlands determined by high resolution multi-temporal topographic surveys. *Catena* **2014**, *120*, 164–176.
35. Wheaton, J.M.; Brasington, J.; Darby, S.E.; Sear, D.A. Accounting for uncertainty in DEMs from repeat topographic surveys: improved sediment budgets. *Earth Surf. Process. Landf. J. Br. Geomorphol. Res. Group* **2010**, *35*, 136–156.
36. Brasington, J.; Vericat, D.; Rychkov, I. Modeling river bed morphology, roughness, and surface sedimentology using high resolution terrestrial laser scanning. *Water Resour. Res.* **2012**, *48*.
37. Bangen, S.; Hensleigh, J.; McHugh, P.; Wheaton, J. Error modeling of DEMs from topographic surveys of rivers using fuzzy inference systems. *Water Resour. Res.* **2016**, *52*, 1176–1193.
38. Lane, S.N.; Chandler, J.H. The generation of high-quality topographic data for hydrology and geomorphology: new data sources, new applications and new problems. *Earth Surf. Process. Landf. J. Br. Geomorphol. Res. Group* **2003**, *28*, 229–230.
39. Milan, D.J.; Heritage, G.L.; Large, A.R.; Fuller, I.C. Filtering spatial error from DEMs: Implications for morphological change estimation. *Geomorphology* **2011**, *125*, 160–171.
40. Passalacqua, P.; Belmont, P.; Staley, D.M.; Simley, J.D.; Arrowsmith, J.R.; Bode, C.A.; Crosby, C.; DeLong, S.B.; Glenn, N.F.; Kelly, S.A.; et al. Analyzing high resolution topography for advancing the understanding of mass and energy transfer through landscapes: A review. *Earth-Sci. Rev.* **2015**, *148*, 174–193.
41. Victoriano, A.; Brasington, J.; Guinau, M.; Furdada, G.; Cabré, M.; Moysset, M. Geomorphic impact and assessment of flexible barriers using multi-temporal LIDAR data: The Portainé mountain catchment (Pyrenees). *Eng. Geol.* **2018**, *237*, 168–180.
42. Brasington, J.; Rumsby, B.; McVey, R. Monitoring and modelling morphological change in a braided gravel-bed river using high resolution GPS-based survey. *Earth Surf. Process. Landf. J. Br. Geomorphol. Res. Group* **2000**, *25*, 973–990.
43. Brasington, J.; Langham, J.; Rumsby, B. Methodological sensitivity of morphometric estimates of coarse fluvial sediment transport. *Geomorphology* **2003**, *53*, 299–316.
44. Lane, S.N.; Westaway, R.M.; Murray Hicks, D. Estimation of erosion and deposition volumes in a large, gravel-bed, braided river using synoptic remote sensing. *Earth Surf. Process. Landf. J. Br. Geomorphol. Res. Group* **2003**, *28*, 249–271.
45. James, M.R.; Robson, S.; Smith, M.W. 3-D uncertainty-based topographic change detection with structure-from-motion photogrammetry: precision maps for ground control and directly georeferenced surveys. *Earth Surf. Process. Landf.* **2017**, *42*, 1769–1788.
46. Nesbit, P.R.; Hugenholtz, C.H. Enhancing UAV–SfM 3D model accuracy in high-relief landscapes by incorporating oblique images. *Remote. Sens.* **2019**, *11*, 239.
47. James, M.R.; Robson, S. Mitigating systematic error in topographic models derived from UAV and ground-based image networks. *Earth Surf. Process. Landf.* **2014**, *39*, 1413–1420.
48. Rossi, R.K. Evaluation of Structure-from-Motion from a Pole-Mounted Camera for Monitoring Geomorphic Change. Ph.D. Thesis, Utah State University, Logan, UT, USA, 2018.
49. Fernández, T.; Pérez, J.L.; Cardenal, J.; Gómez, J.M.; Colomo, C.; Delgado, J. Analysis of landslide evolution affecting olive groves using UAV and photogrammetric techniques. *Remote Sens.* **2016**, *8*, 837.

50. Fernández, T.; Pérez, J.L.; Colomo, C.; Cardenal, J.; Delgado, J.; Palenzuela, J.A.; Irigaray, C.; Chacón, J. Assessment of the evolution of a landslide using digital photogrammetry and LiDAR techniques in the Alpujarras region (Granada, southeastern Spain). *Geosciences* **2017**, *7*, 32.
51. Rumsby, B.; Brasington, J.; Langham, J.; McLelland, S.; Middleton, R.; Rollinson, G. Monitoring and modelling particle and reach-scale morphological change in gravel-bed rivers: Applications and challenges. *Geomorphology* **2008**, *93*, 40–54.
52. Dewitte, O.; Daoudi, M.; Bosco, C.; Van Den Eeckhaut, M. Predicting the susceptibility to gully initiation in data-poor regions. *Geomorphology* **2015**, *228*, 101–115.
53. Martínez-Casasnovas, J. A spatial information technology approach for the mapping and quantification of gully erosion. *Catena* **2003**, *50*, 293–308.
54. Perroy, R.L.; Bookhagen, B.; Asner, G.P.; Chadwick, O.A. Comparison of gully erosion estimates using airborne and ground-based LiDAR on Santa Cruz Island, California. *Geomorphology* **2010**, *118*, 288–300.
55. Nadal-Romero, E.; Revuelto, J.; Errea, P.; López-Moreno, J. The application of terrestrial laser scanner and SfM photogrammetry in measuring erosion and deposition processes in two opposite slopes in a humid badlands area (central Spanish Pyrenees). *Soil* **2015**, *1*, 561.
56. Vandekerckhove, L.; Poesen, J.; Govers, G. Medium-term gully headcut retreat rates in Southeast Spain determined from aerial photographs and ground measurements. *Catena* **2003**, *50*, 329–352.
57. Marzoff, I.; Ries, J.B.; Poesen, J. Short-term versus medium-term monitoring for detecting gully-erosion variability in a Mediterranean environment. *Earth Surf. Process. Landf.* **2011**, *36*, 1604–1623.
58. Ezzaouini, M.A.; Mahé, G.; Kacimi, I.; Zerouali, A. Comparison of the MUSLE Model and Two Years of Solid Transport Measurement, in the Bouregreg Basin, and Impact on the Sedimentation in the Sidi Mohamed Ben Abdellah Reservoir, Morocco. *Water* **2020**, *12*, 1882.
59. Maleval, V.; Pitois, F. Fonctionnement hydro-sédimentaire et bilan sédimentaire du lac de Saint-Germain-de-Confolens (Charente, France): paramètres géomorphologiques à prendre en considération dans la gestion du lac. *Phys.-Géo. Géol. Phys. Environ.* **2017**, 197–227.